Mechanics of Materials 204 (2025) 105275

Contents lists available at ScienceDirect

Mechanics of Materials

journal homepage: www.elsevier.com/locate/mecmat

Research paper

Modelling and finite element simulation of martensite and bainite phase transformations during quenching under consideration of carbon repartitioning

Tim Furlan [a], Markus Schewe [a], Philipp Scherm [a], Philipp Retzl [b], Ernst Kozeschnik [b], Andreas Menzel [a,c,*]

[a] Institute of Mechanics, Department of Mechanical Engineering, TU Dortmund, Leonhard-Euler-Str. 5, 44227 Dortmund, Germany
[b] Institute of Materials Science and Technology, TU Wien, Getreidemarkt 9, Objekt 8, 1060 Wien, Austria
[c] Division of Solid Mechanics, Lund University, P.O. Box 118, 22100 Lund, Sweden

ARTICLE INFO

Dataset link: https://github.com/InstituteOfMechanics/Phase_Trafos_Carbon_Repartitioning

Keywords:
Phase transformations
Carbon repartitioning
High-carbon steel
Quenching
Abaqus
UMAT

ABSTRACT

Control of the microstructure of steel components during their processing is a crucial factor for reaching desired product properties. Realistic simulations of the microstructure evolution during processing can facilitate the improvement of existing processes as well as the design of new ones by reducing the need for time- and cost-intensive experimental investigations. This work focuses on the modelling and advanced simulation of quenching of components made of the high-carbon bearing steels 100Cr6 and 100CrMnSi6-4, during which transformations from austenite to martensite and bainite are considered. Special attention is given to the carbon-enrichment of the austenite phase during the formation of carbide-free bainite, since the change in carbon content also changes the martensite start temperature. A novel model based on the widely used Koistinen–Marburger and Johnson–Mehl–Avrami–Kolmogorov models is proposed, which explicitly takes into account the carbon contents of the remaining austenite and its influence on the kinetics of both transformations. The proposed model is implemented as a user material for the commercial finite element software Abaqus.

Our source code and calibration data are available at https://github.com/InstituteOfMechanics/Phase_Trafos_Carbon_Repartitioning.

1. Introduction

Steel is a versatile material widely used in various industries such as construction, automotive, and tool production. It features a favourable ratio of performance to price, as well as a high recycling rate. Numerical simulations can offer a valuable tool for the prediction of the influence of process parameters on the final product performance, enabling improved product properties and reducing energy and material usage.

The properties and quality of any steel product are determined by a multitude of factors. In conjunction with the chemical composition, the smelting and casting processes determine the initial microstructure of the material, characterised by grain sizes, phase distribution, inclusions and precipitates. Forming and machining processes introduce mechanical and thermal loads, resulting in a heavily process-dependent evolution of the microstructure. Subsequent heat treatments, such as quench hardening, tempering, or annealing, lead to further microstructural evolution. Heat treatment is typically followed by at least one finishing process, introducing another set of mechanical and thermal loads. For any given chemical composition, the material properties, and therefore the material response to any manufacturing process, are determined by the microstructure resulting from all previous production steps.

The fine-tuning of process parameters using trial and error is time-consuming and costly. A possible economic advantage might be offset by the cost of required tests, especially when there are large numbers of rejects. In an industrial setting, process parameters are therefore often chosen with relatively large safety margins, so that neither energy efficiency nor product quality are optimal. Reliable model-based prediction of microstructure evolution during processing can therefore facilitate energy savings and product performance improvements, which would otherwise not be economical to achieve.

This work focuses on modelling the phase evolution during the quench hardening of steel components. During this process, workpieces are heated in an austenitisation furnace above the austenitisation

* Corresponding author at: Division of Solid Mechanics, Lund University, P.O. Box 118, 22100 Lund, Sweden.
E-mail address: andreas.menzel@solid.lth.se (A. Menzel).

https://doi.org/10.1016/j.mechmat.2025.105275
Received 20 September 2024; Received in revised form 26 January 2025; Accepted 27 January 2025
Available online 8 February 2025

temperature, inducing a change from body-centered cubic (BCC) to face-centered cubic (FCC) lattice structure. They are then held at constant temperature for a defined time period, before being cooled down to induce the transformation to martensite. Depending on the cooling rate, a diffusive transformation of austenite to pearlite or bainite may begin before the onset of the martensite transformation, reducing the available fraction of austenite for the martensite transformation.

Extensive overviews on the modelling of quenching processes are given by Gür and Şimşir (2012) and Şimşir and Gür (2016). Although Hunkel (2020) recently showed that the martensite transformation is not solely dependent on the temperature, the assumption of an athermal martensite transformation is frequently and successfully used in the literature. A widely used class of models using this assumption is based on Koistinen and Marburger (1959) and usually referred to as Koistinen–Marburger (KM) models. Various improvements of the model have been proposed for different applications, such as empirical formulae for composition-dependent model parameters to apply the model with reduced calibration effort (Van Bohemen and Sietsma, 2009). It was shown that the agreement of simulation and experiment for individual cases can be improved by the introduction of additional parameters and terms in the model (Lee and Van Tyne, 2012; Huyan et al., 2015; Li et al., 2015).

A popular model for the diffusive transformation was proposed individually by three different groups of researchers and is referred to as the JMAK model (Avrami, 1939, 1940, 1941; Johnson and Mehl, 1939; Kolmogorov, 1937, 1992). While the original JMAK model is intended for the modelling of isothermal processes, it has been widely applied to general temperature paths based on the concept of fractional nucleation proposed by Scheil (1935), also often referred to as additivity in this context. As for the KM model, various extensions and improvements have been published for the JMAK model, such as temperature-dependent parameters (Çetinel et al., 2000) or a dependency of the model parameters on the transformation state (Jia et al., 2010). An extension including the influence of the austenite grain size on the transformation kinetics was proposed by Reti et al. (2001). The JMAK model has also been applied to the austenitisation, e.g. by Li et al. (2016). It should be noted that Leblond and Devaux (1984) showed that the additivity rule is not generally valid when incomplete transformations are considered, and proposed a new model based on the equilibrium phase composition at each temperature. A dependency of the JMAK parameters on the cooling rate was found for high carbon steel by Rezaei et al. (2023).

A drawback of the KM and JMAK models in their original form is the neglected interaction of microstructure evolution with mechanical load and deformation, most importantly the effect of transformation-induced plasticity (TRIP), for which an extensive overview was given by Taleb (2014). At the core, TRIP denotes the occurrence of a non-reversible strain during a phase transformation.

Transformation plasticity has been incorporated into transformation models e.g. by Leblond et al. (1985, 1986), Fischer (1990) and Ganghoffer and Simonsson (1998). The Leblond model has been widely used, and was for example combined with a modified KM model to predict phase transformations in TRIP steels by Suwanpinij et al. (2017). However, it was shown by Taleb and Petit (2006) that the Leblond model is not able to capture all relevant interactions for the case of 15MND5 steel. An alternative macroscopic model, combining macroscopic plasticity and TRIP, was proposed by Schneidt and Mahnken (2008) and Mahnken et al. (2009).

Another interaction between mechanical state and transformations are stress and strain-induced transformations, which have been modelled e.g. by Tjahjanto et al. (2008) and Hazar et al. (2018). Furthermore, Silva et al. (2004) and Mirhosseini et al. (2022) showed that a full coupling between transformation models and heat generation due to plastic dissipation and heat release is desirable for accurate predictions. The influence of the austenite grain size on the kinetics of phase transformations has already been considered in the classic Leblond model, but are still subject to research (Li et al., 2023).

While phenomenological models have been successfully applied to many engineering applications, their consistency with physics is often questionable. Therefore, considerable research has been conducted to derive thermodynamically consistent phase transformation models and appropriate free energy functions (Gurtin, 1983; James, 1986; Müller, 1989; Abeyaratne and Knowles, 1993; Bhattacharyya and Weng, 1994; Ostwald et al., 2012, 2015; Said Schicchi et al., 2019). More recent models are often applied to phase transformations in shape memory alloys, where the transformations potentially occur frequently during the lifetime of a component (Lagoudas et al., 2012; Junker and Hackl, 2014), or during additive manufacturing (Noll et al., 2024).

Although bainite was already discovered in the first half of the 20th century (Davenport and Bain, 1970), the exact mechanisms of its formation are still subject to research (Oka et al., 1990; Ravi et al., 2016; Toloui and Militzer, 2018; Van Bohemen, 2019), especially with regard to the dependency of the transformation kinetics on the chemical composition, see e.g. Fielding (2013) and Wei et al. (2021). It is however generally accepted that bainite forms into different variants at different temperatures (upper and lower bainite). Furthermore, under appropriate conditions, the formation of carbide-free bainite is possible, where the surplus carbon from the newly formed bainite is repartitioned and enriches the austenite phase (Caballero, 2012).

An overview of models which consider the bainite transformation as displacive was given by Santofimia et al. (2006). Especially the model by Ravi et al. (2016) accounts for the redistribution of carbon during the formation of bainite, while Ravi et al. (2020) investigates the influence of austenite–martensite interfaces as nucleation sites for bainite formation. Empirical formulae have been proposed by Ingber and Kunert (2022) and Van Bohemen (2012) to predict the parameters of the KM model based on the chemical composition, while Kaymak (2007), Mustak et al. (2016) and Hunkel (2020) present experimental results for the steel grades considered in the present work. For the same steel grades, the influence of the austenitisation process on cementite dissolution is investigated experimentally and numerically in Cui et al. (2017).

Effective (macroscopic) material properties are predicted from a given microstructure by homogenisation. Different methods are discussed by Andersson et al. (2022), while Fernández-Pisón et al. (2024) applied incremental mean-field homogenisation on martensite transformations. The microstructure is considered in detail by Amirmaleki et al. (2016), who applied the representative volume element method to predict material properties, by Boccardo et al. (2017), who used different representative volume elements to incorporate the morphology of the different phases into the transformation kinetics, and by Hellebrand et al. (2023), who investigated the influence of the microstructure distribution in representative volume elements on residual stress distribution.

This work presents a novel framework to integrate the repartitioning of carbon during the formation of bainite with phenomenological transformation models. Bearing steels 100Cr6 and 100CrMnSi6-4 are considered for the presented academic examples, where it is assumed that the higher silicone content of the latter grade at least partially suppresses carbide formation, and therefore austenite is enriched in carbon, which leads to an incomplete bainite transformation as also described in Tsuzaki and Maki (1995). Since Woodard et al. (1999), Şimşir and Gür (2008) and De Oliveira et al. (2010) found good results for similar applications, the classical KM model is applied for the martensite transformation, while the bainite transformation is based on a JMAK model. Comparatively simple variants of both models were chosen due to the focus of this work on the modelling of the carbon partitioning and due to the lack of adequate calibration data for the more complex models. The calibration procedure for both models is presented in detail, including the generation of temperature-dependent parameters for the JMAK model. Based on simulations in MatCalc (Kozeschnik, 2022), the change of transformation kinetics due to the carbon enrichment during the formation of carbide-free bainite is included in the model. Finally, an implementation of the model for a commercial finite element software is presented, which is made publicly available with this work.

2. Simulation framework and phase transformation model

A thermomechanically coupled finite element formulation is proposed to model the quenching process. The material model is able to predict the evolution of phase volume fractions, strains, stresses, thermal flow, and the carbon content of each phase under prescribed thermal and mechanical loading. The mechanical problem is formulated in the geometrically linearised setting, assuming small deformations. Phenomenological models are used for the decomposition of austenite into martensite and bainite/austenite–martensite and austenite–bainite transformations due to the additional effort required for the calibration and solving of more complicated models.

The proposed model is based on the model introduced by De Oliveira et al. (2010), but takes into account the carbon content of each individual phase, making these quantities available as variables in phase transformation models. Evolution equations for the carbon content are derived for transformations with and without carbon repartitioning.

2.1. Simulation framework

For the study of boundary-value problems, the model proposed in this work is implemented in a quasi-static, thermodynamically coupled finite element framework. Assuming conservation of mass, the coupled problem is defined by the quasi-static balance of linear momentum

$$\nabla \cdot \boldsymbol{\sigma} + \boldsymbol{b} = \boldsymbol{0} \ , \tag{1}$$

and the first law of thermodynamics

$$\rho \, c_\mathrm{p} \, \dot{T} + \nabla \cdot \boldsymbol{q} - r = 0 \ , \tag{2}$$

where $\boldsymbol{\sigma}$ denotes the (Cauchy) stresses, $\boldsymbol{b}$ represents mass-specific volumetric loads, ρ denotes the mass density, c_p denotes the specific heat capacity, $\boldsymbol{q}$ denotes the heat flux, r represents volume-specific heat sources, and the notation $\dot{\bullet}$ represents the time derivative of a quantity $\bullet$. In the following, Eqs. (1) and (2) will be referred to as the *mechanical* and *thermal* problem, respectively.

At each material point, a coexistence of an austenite phase, a martensite phase, and a bainite phase is assumed, and their respective volume fractions are denoted by β_A, β_M, and β_B, respectively.

The material point represents a small homogeneous volume v with mass m. Denoting the density for each phase as ρ_i, the mass contribution of each phase can be expressed as

$$m_i = \rho_i \, \beta_i \, v \ . \tag{3}$$

The *metallurgical problem* is defined by the mass balance

$$\sum_i m_i = m \Leftrightarrow \sum_i \frac{\rho_i}{\rho} \, \beta_i = 1 \ . \tag{4}$$

A common assumption in the small strain setting is that the density changes between phases are small, i.e. $\rho_i \approx \rho$, which leads to

$$\sum_i \beta_i = 1 \ . \tag{5}$$

The *chemical problem* is defined by the mass balance for each element of the alloy. However, since the carbon content is expected to have the largest impact on the transformation kinetics, in this work only the carbon mass balance is considered. For the material point, the total mass of carbon is given by

$$m_\mathrm{C} = \rho \, v \, x_\mathrm{C} \ , \tag{6}$$

in terms of the nominal carbon content x_C, while the mass of carbon stored in each phase reads

$$\begin{aligned} m_{\mathrm{C,A}} &= \rho \, v \, \beta_\mathrm{A} \, x_{\mathrm{C,A}} \ , \\ m_{\mathrm{C,M}} &= \rho \, v \, \beta_\mathrm{M} \, x_{\mathrm{C,M}} \ , \\ m_{\mathrm{C,B}} &= \rho \, v \, \beta_\mathrm{B} \, x_{\mathrm{C,B}} \ , \end{aligned} \tag{7}$$

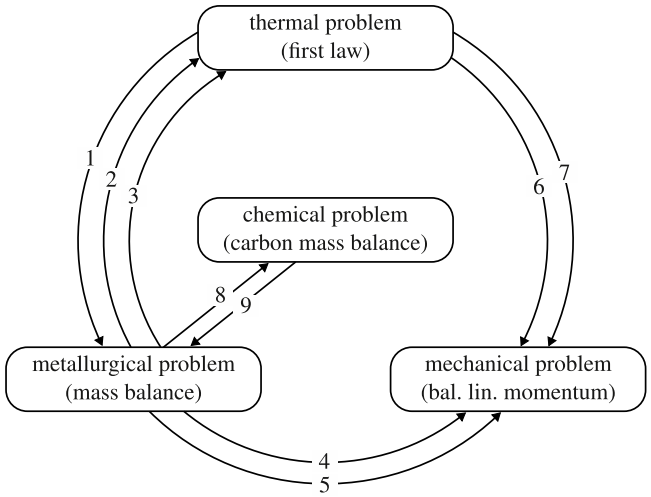

1 Thermal driving force for phase transformations
2 Phase-dependent thermal properties
3 Latent heat of transformations
4 Phase-dependent mechanical properties
5 Transformation strains
6 Thermal strains
7 Temperature-dependent mechanical properties
8 Carbon enrichment of austenite during bainitic transformation
9 Transformation laws dependent on carbon content

Fig. 1. Overview of the problems and their interactions considered in the model. Under these assumptions, the mechanical problem does not influence the solution of the other three problems, and can therefore be solved individually as a post-processing step to the coupled solution of the thermal, chemical, and metallurgical problems. Dependencies which are considered constant during a simulation, e.g. the dependency of all material parameters on the overall chemical composition, are not depicted.

where $x_{\mathrm{C},i}$ denotes the carbon content of phase i. The carbon mass balance then reads

$$m_\mathrm{C} = m_{\mathrm{C,A}} + m_{\mathrm{C,M}} + m_{\mathrm{C,B}} \ . \tag{8}$$

Due to the limited time at elevated temperature, diffusional transport of carbon is neglected in the presented model. The primary global unknowns in the finite element problem are the displacement field $\boldsymbol{u}$ and therefore the temperature field T, while the volume fractions β_i and carbon contents $x_{\mathrm{C},i}$ represent (local) internal variables at each material point. Since the deformations associated with phase transformations are usually small in comparison with the part dimensions, the mechanical behaviour is modelled as *geometrically linear*, i.e. the strains $\boldsymbol{\varepsilon}$ are defined in terms of the displacement field $\boldsymbol{u}$ as

$$\boldsymbol{\varepsilon} = \frac{1}{2} \left[\nabla \boldsymbol{u} + [\nabla \boldsymbol{u}]^\mathrm{t} \right] \ . \tag{9}$$

Within the finite element framework, the material response must be defined in terms of appropriate constitutive models of the form

$$\boldsymbol{\sigma} \left(\boldsymbol{\varepsilon}, T, \beta_i, x_{\mathrm{C},i} \right) \ , \tag{10}$$

$$\boldsymbol{q} \left(\boldsymbol{\varepsilon}, T, \nabla T, \beta_i, x_{\mathrm{C},i} \right) \ , \tag{11}$$

$$r \left(\boldsymbol{\varepsilon}, T, \beta_i, x_{\mathrm{C},i} \right) \ , \tag{12}$$

together with heat capacity and evolution equations for all internal variables β_i and $x_{\mathrm{C},i}$. A graphical overview of the problems and interactions which are considered in the model is presented in Fig. 1.

2.2. Strains and stresses

In general, strains and stresses in different phases are expected to be non-uniform and need to be considered separately. For the sake of simplicity, the linear mixture rule is applied instead of a more rigorous homogenisation scheme, i.e. the model is formulated only in terms of effective macroscopic quantities which are obtained from the averaging of the respective quantities for the individual phases.

Following e.g. De Oliveira et al. (2010), an additive decomposition for the strain increment $\mathrm{d}\boldsymbol{\varepsilon}$ is assumed and reads

$$\mathrm{d}\boldsymbol{\varepsilon} = \mathrm{d}\boldsymbol{\varepsilon}^{\mathrm{el}} + \mathrm{d}\boldsymbol{\varepsilon}^{\mathrm{th}} + \mathrm{d}\boldsymbol{\varepsilon}^{\mathrm{tv}} \,, \tag{13}$$

where $\mathrm{d}\boldsymbol{\varepsilon}^{\mathrm{el}}$ denotes the elastic strain increment, $\mathrm{d}\boldsymbol{\varepsilon}^{\mathrm{th}} = \alpha\, \boldsymbol{I}\, \mathrm{d}T$ denotes the thermal expansion due to the thermal expansion coefficient α and a temperature increment $\mathrm{d}T$,[1] and $\mathrm{d}\boldsymbol{\varepsilon}^{\mathrm{tv}} = \mathrm{d}\gamma\, \boldsymbol{I}$ is a volumetric transformation strain increment, where the linear strain increment due to transformations is given by $\mathrm{d}\gamma$. Moreover, $\boldsymbol{I}$ represents the second-order identity tensor.

Following Hooke's law, the stresses $\boldsymbol{\sigma}$ are calculated as

$$\boldsymbol{\sigma} = \mathbf{E} : \boldsymbol{\varepsilon}^{\mathrm{el}} \,, \tag{14}$$

where the (Cartesian) coefficients of the fourth-order elasticity tensor $\mathbf{E}$ read

$$\mathsf{E}_{ijkl} = \frac{E\nu}{[1+\nu][1-2\nu]}\, \delta_{ij}\, \delta_{kl} + \frac{E}{2[1+\nu]} \left[\delta_{ik}\, \delta_{jl} + \delta_{il}\, \delta_{jk}\right] \tag{15}$$

in terms of Young's modulus E, Poisson's ratio ν, and the Kronecker delta δ_{ij}. Considering an explicit dependency on the temperature T for all quantities in each individual phase, averaging by the linear mixture rule yields

$$E(T,\, \beta_i) = \sum_i \beta_i\, E_i(T) \,, \tag{16}$$

$$\nu(T,\, \beta_i) = \sum_i \beta_i\, \nu_i(T) \,, \tag{17}$$

$$\alpha(T,\, \beta_i) = \sum_i \beta_i\, \alpha_i(T) \,. \tag{18}$$

The transformation strain increment is computed based on the transformation strains γ_i for each phase as

$$\mathrm{d}\gamma(T,\, \beta_i) = \sum_i \gamma_i(T)\, \mathrm{d}\beta_i \,. \tag{19}$$

It is remarked that the homogenisation was performed by a linear mixture rule, which here is equivalent to the Taylor–Voigt homogenisation assumption. The approach is chosen for the sake of simplicity, although alternative homogenisation schemes, such as the Reuss-Sachs approach or more advanced relaxation frameworks, are expected to yield more accurate results. Furthermore, any influence of the stress state on the phase transformations is neglected in the model, since no external tractions are applied during the quenching process.

2.3. Heat transfer

The well-established isotropic Fourier's law

$$\boldsymbol{q} = -\Lambda\, \nabla T \tag{20}$$

is assumed for the heat transfer problem, where the isotropic thermal conductivity Λ is considered to be a function of the temperature. Linear mixture is again applied to average the thermal parameters, i.e.

$$c_{\mathrm{p}}(T,\, \beta_i) = \sum_i \beta_i\, c_{\mathrm{p},i}(T) \,, \tag{21}$$

$$\Lambda(T,\, \beta_i) = \sum_i \beta_i\, \Lambda_i(T) \,. \tag{22}$$

[1] A reference temperature T_0 has to be chosen when evaluating the thermal strain in this formulation.

Robin-type boundary conditions

$$-\boldsymbol{q} \cdot \boldsymbol{n} = h\,[T - T_\infty] + e\, k_{\mathrm{B}}\, [T^4 - T_\infty^4] \tag{23}$$

are used to model the heat flux from a surrounding medium of temperature T_∞ through a boundary with outward normal vector $\boldsymbol{n}$. Within the finite element framework, the surface heat flux enters the heat Eq. (20) as a surface contribution. Convectional heat exchange is governed by the temperature-dependent heat transfer coefficient (HTC), denoted by h, while heat exchange by radiation is determined by the emissivity e and the Boltzmann constant k_{B}.

2.4. Evolution of carbon content

After inserting Eq. (7), the rate form of the diffusionless carbon mass balance (8) reads

$$\dot{\beta}_{\mathrm{A}}\, x_{\mathrm{C,A}} + \beta_{\mathrm{A}}\, \dot{x}_{\mathrm{C,A}} + \dot{\beta}_{\mathrm{M}}\, x_{\mathrm{C,M}} + \beta_{\mathrm{M}}\, \dot{x}_{\mathrm{C,M}} + \dot{\beta}_{\mathrm{B}}\, x_{\mathrm{C,B}} + \beta_{\mathrm{B}}\, \dot{x}_{\mathrm{C,B}} = 0 \,. \tag{24}$$

To derive evolution equations for the unknown carbon content in each phase, two additional simplifying assumptions are introduced. It is assumed that martensite always forms with the same amount of carbon that is currently present in the parent austenite phase, i.e.

$$\dot{m}_{\mathrm{C,M}} = \dot{m}_{\mathrm{M}}\, x_{\mathrm{C,A}} \,. \tag{25}$$

Using the product rule, this equation expands to

$$\dot{\beta}_{\mathrm{M}}\, x_{\mathrm{C,M}} + \beta_{\mathrm{M}}\, \dot{x}_{\mathrm{C,M}} = \dot{\beta}_{\mathrm{M}}\, x_{\mathrm{C,A}} \,. \tag{26}$$

The second assumption is that the carbon content in the bainite phase is constant and independent of the evolution in the parent phase, so that

$$\dot{x}_{\mathrm{C,B}} = 0 \tag{27}$$

holds. In the following, $x_{\mathrm{C,B}}$ is thus treated as a constant parameter. It is remarked that the bainite phase carbon concentration was shown to depend on the temperature during the transformation for different steel grades, see Benrabah et al. (2024). This effect is neglected in the proposed model since it is especially pronounced at lower temperatures, where martensitic transformation is expected to be dominant during quenching. Inserting Eq. (26) and (27) into Eq. (24) yields the evolution equation

$$\dot{x}_{\mathrm{C,A}} = -\frac{\dot{\beta}_{\mathrm{A}} x_{\mathrm{C,A}} + \dot{\beta}_{\mathrm{M}} x_{\mathrm{C,A}} + \dot{\beta}_{\mathrm{B}} x_{\mathrm{C,B}}}{\beta_{\mathrm{A}}} \,, \tag{28}$$

for the carbon content of the austenite phase. Using Eq. (5), the evolution equation can also be expressed as

$$\dot{x}_{\mathrm{C,A}} = \frac{\dot{\beta}_{\mathrm{B}}}{\beta_{\mathrm{A}}} \left[x_{\mathrm{C,A}} - x_{\mathrm{C,B}}\right] \,. \tag{29}$$

The derived result does not depend on the reference volume introduced to motivate the equations, and is therefore directly applicable to the quadrature point level in the finite element model. It should be noted that Eq. (29) reduces to $\dot{x}_{\mathrm{C,A}} = 0$ if $x_{\mathrm{C,B}} = x_{\mathrm{C,A}}$. In this case, all phases exhibit the same carbon content, and the carbon mass balance is trivially fulfilled.

2.5. Austenite–martensite transformation

Martensite formation is modelled by the Koistinen–Marburger (KM) model (Koistinen and Marburger, 1959). The evolution of the martensite volume fraction is assumed to be dependent only on the temperature T and is given by the equation

$$\beta_{\mathrm{M}} = 1 - \exp\left(-k\left[M_{\mathrm{S}} - T\right]\right) \,, \tag{30}$$

where M_{S} denotes the martensite start temperature and k is called the rate parameter. Reformulating the original KM model as a rate equation,

and interpreting the term $\left[1-\beta_{\mathrm{M}}\right]$ as the remaining austenite volume fraction β_{A}, yields the expression

$$\begin{aligned}\dot{\beta}_{\mathrm{M}} &= -\exp\left(-k\left[M_{\mathrm{S}}-T\right]\right) k\,\dot{T} \\ &= -\left[1-\beta_{\mathrm{M}}\right] k\,\dot{T} = -\beta_{\mathrm{A}}\, k\,\dot{T}\ ,\end{aligned} \tag{31}$$

which remains valid even if competing diffusional transformations of austenite to bainite occur.

To ensure that the martensitic transformation takes place only below the martensite start temperature M_{S}, the term $\mathrm{H}\left(M_{\mathrm{S}}-T\right)$ is introduced, where H denotes the Heaviside function. Since the transformation of martensite back to austenite is not included in the model, another Heaviside term $\mathrm{H}\left(-\dot{T}\right)$ is introduced to restrict the transformation direction. After introducing an activation function

$$\zeta_{\mathrm{M}} = \mathrm{H}\left(M_{\mathrm{S}}-T\right)\mathrm{H}\left(-\dot{T}\right)\ , \tag{32}$$

which aggregates the conditions for an evolution, the final rate equation for the martensite volume fraction reads

$$\dot{\beta}_{\mathrm{M}} = -\zeta_{\mathrm{M}}\,\beta_{\mathrm{A}}\,k\,\dot{T}\ . \tag{33}$$

2.6. Austenite–bainite transformation

The transformation of austenite to bainite is modelled based on the classic JMAK model developed by Johnson and Mehl (Johnson and Mehl, 1939; Barmak, 2018), Avrami (Avrami, 1939, 1940, 1941), and Kolmogorov (Kolmogorov, 1937, 1992), which describes the isothermal transformation kinetics by an equation of the type

$$\beta_{\mathrm{B}} = \hat{\beta}_{\mathrm{B}}\left[1-\exp\left(-b\,t^{N}\right)\right]\ , \tag{34}$$

where $\hat{\beta}_{\mathrm{B}}$ denotes the maximum reachable volume fraction of bainite. It is assumed that the model parameters b and N are functions of the temperature T. The transformation rate reads

$$\begin{aligned}\dot{\beta}_{\mathrm{B}} &= \hat{\beta}_{\mathrm{B}}\, N\, b\, t^{N-1}\exp\left(b\,t^{N}\right) \\ &= N\, b\, t^{N-1}\left[\hat{\beta}_{\mathrm{B}}-\beta_{\mathrm{B}}\right]\ .\end{aligned} \tag{35}$$

Solving Eq. (34) for the time t leads to the expression

$$t^{*} = \left[\frac{1}{b}\ln\left(\frac{\hat{\beta}_{\mathrm{B}}}{\hat{\beta}_{\mathrm{B}}-\beta_{\mathrm{B}}}\right)\right]^{\frac{1}{N}}\ , \tag{36}$$

which can be interpreted as the time required to reach a given bainite volume fraction β_{B} on an isothermal path, sometimes called the *fictitious time*. Inserting Eq. (36) into Eq. (35), and introducing an activation function

$$\zeta_{\mathrm{B}} = \mathrm{H}\left(B_{\mathrm{S}}-T\right)\ , \tag{37}$$

in terms of the bainite start temperature B_{S}, yields

$$\dot{\beta}_{\mathrm{B}} = \zeta_{\mathrm{B}}\, N\, b^{\frac{1}{N}}\left[\hat{\beta}_{\mathrm{B}}-\beta_{\mathrm{B}}\right]\left[\ln\left(\frac{\hat{\beta}_{\mathrm{B}}}{\hat{\beta}_{\mathrm{B}}-\beta_{\mathrm{B}}}\right)\right]^{\frac{N-1}{N}}\ , \tag{38}$$

eliminating the explicit time dependency.

Although the JMAK model is originally intended for isothermal applications, it can be employed for general temperature paths by assuming a series of isothermal steps at varying temperatures, as shown in e.g. De Oliveira et al. (2010). A parametrisation for the model parameters b and N dependent on the temperature is then required.

It is remarked that the JMAK model Eq. (38) in rate form is valid only after the onset of the bainite transformation, since the rate for the bainite volume fraction is zero in case no bainite has been formed. Application of the time-dependent rate form Eq. (35) requires tracking of the time of the onset of transformation. An alternative approach, based on the concept of fractional nucleation introduced in Scheil (1935), is therefore used to model the incubation, i.e. the evolution of the first 1% of bainite. Following Scheil (1935), the incubation for a general temperature path is assumed to be complete at temperature T_x if the condition

$$\int_{T_0}^{T_x}\frac{\mathrm{d}T}{\dot{T}\,\tau(T)} = 1 \tag{39}$$

is fulfilled, where T_0 is an equilibrium temperature at which no nucleation occurs, and $\tau(T)$ denotes the nucleation time for an isothermal path at temperature T, which can be acquired from e.g. isothermal time–temperature–transformation (TTT) diagrams. Given an explicit parametrisation $b(T)$ and $N(T)$, the nucleation time can be obtained from Eq. (36) as

$$\tau\left(T\right) = \left[\frac{1}{b\left(T\right)}\ln\left(\frac{1}{0.99}\right)\right]^{\frac{1}{N(T)}}\ . \tag{40}$$

Eq. (39) is scaled to 1% to represent the bainite fraction during incubation, leading to the expression

$$\beta_{\mathrm{B}} = 0.01\int\frac{1}{\tau\left(T\right)}\,\mathrm{d}t\ , \tag{41}$$

or, in rate form,

$$\dot{\beta}_{\mathrm{B}} = 0.01\,\frac{1}{\tau\left(T\right)}\ . \tag{42}$$

Combining the models for nucleation and further evolution of the bainite volume fraction yields

$$\dot{\beta}_{\mathrm{B}} = \begin{cases} 0.01\,\zeta_{\mathrm{B}}/\tau & \text{if } \beta_{\mathrm{B}} \le 1\% \\ \zeta_{\mathrm{B}}\, N\, b^{\frac{1}{N}}\left[\hat{\beta}_{\mathrm{B}}-\beta_{\mathrm{B}}\right]\left[\ln\left(\frac{\hat{\beta}_{\mathrm{B}}}{\hat{\beta}_{\mathrm{B}}-\beta_{\mathrm{B}}}\right)\right]^{\frac{N-1}{N}} & \text{if } \beta_{\mathrm{B}} > 1\% \end{cases}\ . \tag{43}$$

To complete the model for the bainite evolution, the maximum reachable bainite fraction $\hat{\beta}_{\mathrm{B}}$ has to be specified. It is assumed that a function $\mathrm{f}(T, x_{\mathrm{C,A}})$ exists which describes the amount of bainite that will form from the current amount of austenite for a given temperature and carbon content. This function returns the value 1 if, assuming infinite transformation time, a complete transformation to bainite occurs. The maximum reachable bainite fraction then reads

$$\hat{\beta}_{\mathrm{B}} = \mathrm{f}\left(T, x_{\mathrm{C,A}}\right)\beta_{\mathrm{A}} + \beta_{\mathrm{B}}\ , \tag{44}$$

where β_{B} denotes the bainite currently present.

For a given temperature T^{*}, current carbon content in the austenite phase $x_{\mathrm{C,A}}$, and prescribed carbon content in the bainite phase $x_{\mathrm{C,B}}$, the function f is chosen based on a lever rule. Assuming a monotonous function $B_{\mathrm{S}}(x_{\mathrm{C,A}})$ for the bainite start temperature, $x^{*}_{\mathrm{C,A}} = B_{\mathrm{S}}^{-1}(T^{*})$ describes the austenite phase carbon content at which no further bainite transformation occurs.

For a hypothetical isothermal evolution of only the current austenite phase to bainite, the resulting phase fractions are denoted by $\tilde{\beta}_{\mathrm{A}}$ and $\tilde{\beta}_{\mathrm{B}}$, respectively. During this hypothetical evolution, the mass balance yields

$$\tilde{\beta}_{\mathrm{A}} + \tilde{\beta}_{\mathrm{B}} = \beta_{\mathrm{A}}\ , \tag{45}$$

and the mass balance for the carbon initially bound in the austenite phase reads

$$\tilde{x}_{\mathrm{C,A}}\,\tilde{\beta}_{\mathrm{A}} + \tilde{x}_{\mathrm{C,B}}\,\tilde{\beta}_{\mathrm{B}} = x_{\mathrm{C,A}}\,\beta_{\mathrm{A}}\ , \tag{46}$$

where $\tilde{x}_{\mathrm{C,A}}$ and $\tilde{x}_{\mathrm{C,B}}$ describe the carbon content of the respective phases after the transformation. Assuming that $x_{\mathrm{C,B}}$ is constant, and that the transformation stops when the condition $\tilde{x}_{\mathrm{C,A}} = x^{*}_{\mathrm{C,A}}$ is fulfilled, inserting Eq. (45) in Eq. (46) yields

$$\mathrm{f}\left(T, x_{\mathrm{C,A}}\right) = \frac{\tilde{\beta}_{\mathrm{B}}}{\beta_{\mathrm{A}}} = \frac{x_{\mathrm{C,A}} - x^{*}_{\mathrm{C,A}}\left(T\right)}{x_{\mathrm{C,B}} - x^{*}_{\mathrm{C,A}}\left(T\right)}\ . \tag{47}$$

A graphical representation of these relations is shown in Fig. 2.

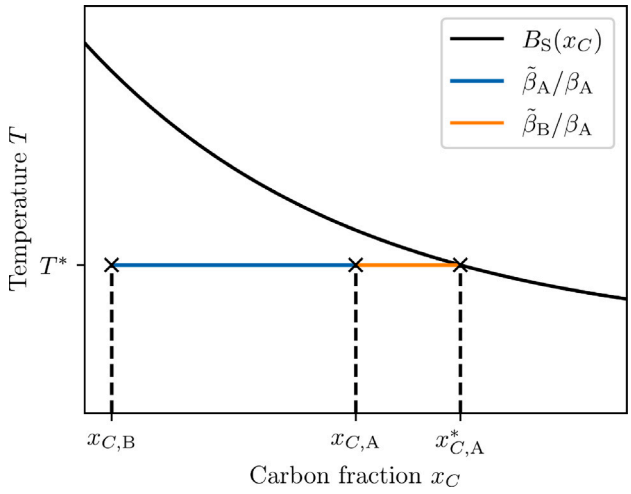

Fig. 2. Graphical representation of the lever rule used to determine the maximum fraction of austenite transforming to bainite at a given temperature. At current temperature T^*, the austenite phase has the current carbon concentration $x_{C,A}$. During a hypothetical isothermal transformation, bainite forms with the prescribed carbon content $x_{C,B}$, inducing carbon enrichment of the remaining austenite. When the carbon content in the remaining austenite reaches the limit value $x^*_{C,A}$, no further transformation takes place, i.e. the bainite phase fraction $\tilde{\beta}_B$ with carbon concentration $x_{C,B}$ and the austenite phase fraction $\tilde{\beta}_A$ with carbon concentration $x^*_{C,A}$ are in equilibrium.

2.7. Parametrisation of the bainite transformation model

Time–temperature–transformation (TTT) diagrams are commonly used to visualise the temperature-dependent start and end times of isothermal transformations, usually in terms of lines for 1% and 99% transformation at each temperature. As stated in Section 2.6, the parameters $b(T)$ and $N(T)$ must be temperature-dependent to model the impact of varying temperature on the transformation kinetics. In this work, the quadratic polynomial ansatz

$$\begin{aligned} \ln(b_p(T)) &= p_{b,0} + p_{b,1}\,T + p_{b,2}T^2 \,, \\ N_p(T) &= p_{N,0} + p_{N,1}T + p_{N,2}T^2 \end{aligned} \tag{48}$$

is used, where the vector $\boldsymbol{p} = \left[p_{b,0},\, p_{b,1},\, p_{b,2},\, p_{N,0},\, p_{N,1},\, p_{N,2}\right]^{\mathrm{t}}$ consists of the constant polynomial coefficients. The prediction for the bainite phase fraction in an isothermal transformation then reads

$$\beta_{B,p}(t,T) = 1 - \exp\left(-b_p(T)\, t^{N_p(T)}\right) \,. \tag{49}$$

A web-based plot digitising tool WebPlotDigitizer (Rohatgi, 2024) was applied to a TTT–diagram of the bainite transformation for 100Cr6, which was published in Kaymak (2007). The times $t_{1,i}$ and $t_{99,i}$, at which the transformation to bainite reaches 1% and 99%, were extracted for a set of discrete temperatures T_i. Optimal parameters $\boldsymbol{p}^*$ were obtained from the nonlinear least-squares optimisation

$$\boldsymbol{p}^* = \arg\min_{\boldsymbol{p}} \sum_i^m \left[\left[\beta_{B,p}(t_{1,i}, T_i) - 0.01\right]^2 + \left[\beta_{B,p}(t_{99,i}, T_i) - 0.99\right]^2 \right] \,. \tag{50}$$

It is remarked that especially the choice of initial guess for the minimisation process is not trivial, and therefore discussed in more detail in Appendix A.1. The optimisation was implemented in Python, and the source code, along with the point data extracted from the diagram, is available in the github repository accompanying this work. An application to other materials, provided the TTT–diagram is available, as well as the application of a higher order polynomial ansatz, is straight-forward by using the provided code.

2.8. Dependency of transformation parameters on chemical composition

In general, the transformation models described in Sections 2.5 and 2.6 have to be calibrated for each material, i.e. for each chemical composition. However, calibration data such as TTT–diagrams is usually not available for every unique material. Especially the influence of slight changes in composition, such as the carbon enrichment during transformation to carbide-free bainite, cannot directly be inferred from the available diagrams. For the proposed model, the JMAK parameters, i.e. b and N, are assumed to be independent of the carbon concentration, and to be identical for both materials under considerations. Therefore, a single TTT-diagram is used for the calibration procedure described in Section 2.7.

For the dependency of the KM model parameters, the empirical equations

$$\begin{aligned} M_S^{(1)} = {} & 530.2 - 290.3\,x_C - 35.5\,x_{Mn} - 6.8\,x_{Si} - 20.8\,x_{Cr} \\ & - 17.2\,x_{Ni} - 10.4\,x_{Mo} + 7.1\,x_{Al} + 4.8\,x_{Co} \\ & - 75\,\left[1 - \exp(-0.96\,x_C)\right] \,, \end{aligned} \tag{51}$$

proposed in Ingber and Kunert (2022) for the martensite start temperature M_S, and

$$\begin{aligned} k^{(1)} = {} & \big[27.2 - 0.14\,x_{Mn} - 0.21\,x_{Si} - 0.11\,x_{Cr} - 0.08\,x_{Ni} \\ & - 0.05\,x_{Mo} - 19.8\,\left[1 - \exp(-1.56\,x_C)\right]\big]/1000 \,, \end{aligned} \tag{52}$$

given in Van Bohemen (2012) for the rate parameter k have been evaluated for the nominal chemical composition of 100Cr6 and 100CrMnSi6-4, defined by Deutsches Institut für Normung e.V. (2023). Table 1 presents the assumed composition and resulting values.

While the resulting rate parameters $k = 0.0112$ and $k = 0.0110$ are in good agreement with the value $k = 0.0109$ estimated in Mustak et al. (2016), the resulting martensite start temperatures $M_S = 150.2\,°C$ and $M_S = 102.1\,°C$ show a significant deviation from literature values. For 100Cr6, Kaymak (2007) finds a value of $M_S = 215\,°C$, and Hunkel (2020) gives $M_S = 212\,°C$. Depending on the austenitisation temperature, Cui et al. (2017) provides values of approximately $M_S = 190\,°C$ to $310\,°C$ for 100Cr6 and $M_S = 190\,°C$ to $280\,°C$ for 100CrMnSi6-4.

Since the literature values suggest that the calculation of the transformation start temperature through Eq. (51) is not accurate for the chemical compositions under consideration, the thermokinetic software package MatCalc 6 (version 6.04.1004) with the thermodynamic database mc_fe.tdb (version 2.060) was used to calculate the start temperatures M_S and B_S for the martensite and bainite transformations, for both 100Cr6 and 100CrMnSi6-4, and for varying carbon content x_C. For the calculations the so called T0-principle was employed. This approach is based on the assumption that diffusionless transformations can only take place at temperatures below the temperature at which the initial and product phases with identical composition possess the same (value of) free energy. Depending on the amount of shear stress occurring during the transformation and the change in molar volume, an additional empirical term considering the necessary mechanical energy has to be added. For the results shown in Fig. 3 an additional energy of $1400\,\mathrm{J\,mol^{-1}}$ was considered for martensite and $400\,\mathrm{J\,mol^{-1}}$ for bainite. Further details and a comparison of this approach with empirical equations for a steel with weight percentages $x_{Si} = 1.5\%$ and $x_{Mn} = 1.5\%$ can be found in Retzl et al. (2021). A linear regression shows good accordance with all data points for carbon contents between 0.5% and 1.5%, as presented in Fig. 3.

For the final model, the start temperatures calculated in MatCalc are combined with Eq. (52). All parametrisations are summarised in Table 2.

2.9. Latent heat of transformations

The latent heat associated with the transformations from austenite to martensite and from austenite to bainite is incorporated into Eq. (2) in terms of the heat source r, as proposed in e.g. Fernandes et al. (1985), Denis et al. (1987) and Woodard et al. (1999), as

$$r = \rho \sum_i \dot{\beta}_i\, \Delta h_i \,, \tag{53}$$

where Δh_i is the specific enthalpy difference of phase i with respect to the austenite phase.

Table 1
Mass fraction of chemical elements in 100Cr6 and 100CrMnSi6-4, following Deutsches Institut für Normung e.V. (2023), along with martensite start temperature $M_S^{(1)}$ and rate coefficient $k^{(1)}$ calculated by Eqs. (51) and (52).

Material	x_C	x_{Si}	x_{Mn}	x_{Cr}	x_{Mo}	x_{Ni}	x_{Al}	x_{Co}	$M_S^{(1)}$	$k^{(1)}$
100Cr6	1.0%	0.25%	0.35%	1.375%	0.1%	0.0%	0.05%	0.0%	150.2 °C	0.0113 °C^{-1}
100CrMnSi6-4	1.0%	0.6%	1.55%	1.525%	0.1%	0.0%	0.05%	0.0%	102.1 °C	0.0110 °C^{-1}

Table 2
Parametrisation for the composition-dependent model parameters M_S, k, and B_S. The transformation start temperatures are obtained from MatCalc simulations, while the rate parameter is calculated based on Eq. (52).

Parameter	Material	Parametrisation	Value at $x_C = 1\%$
M_S	100Cr6	$526.29 - 29\,702.0\, x_C$	229.28 °C
	100CrMnSi6-4	$492.71 - 28\,290.6\, x_C$	209.80 °C
k	100Cr6	$7.14\,\text{e}{-3} + 0.0198 \exp(-156.0\, x_C)$	0.0113
	100CrMnSi6-4	$6.88\,\text{e}{-3} + 0.0198 \exp(-156.0\, x_C)$	0.0110
B_S	100Cr6	$681.51 - 29\,618.0\, x_C$	385.33 °C
	100CrMnSi6-4	$646.95 - 28\,142.8\, x_C$	365.52 °C

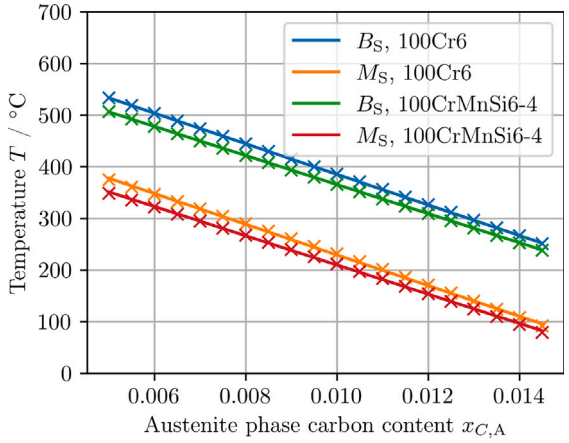

Fig. 3. Martensite and bainite start temperatures for 100Cr6 and 100CrMnSi6-4 dependent on nominal carbon content x_C. Markers represent simulation results obtained from the software MatCalc, while solid lines show the linear regression for each of the data sets.

Table 3
Order of state variables s in user subroutines UMAT and UMATHT. The internal variables $\boldsymbol{\kappa}$ are extracted from the vector s for each subroutine call. Positions 7–9 are used to transfer the temperature derivatives of the internal variables $\boldsymbol{\kappa}$ from UMAT to UMATHT.

Position	Symbol	Description
1	β_M	Martensite volume fraction
2	β_B	Bainite volume fraction
3	β_A	Austenite volume fraction
4	$x_{C,A}$	Austenite phase carbon content
5	$\int \alpha \, dT$	Linear thermal strain
6	$\int d\gamma$	Linear transformation strain
7	$\frac{d\beta_M}{dT}$	Temperature derivative of martensite fraction
8	$\frac{d\beta_B}{dT}$	Temperature derivative of bainite fraction
9	$\frac{dx_{C,A}}{dT}$	Temperature derivative of austenite phase carbon content
10	f	Factor for incomplete bainite transformation

3. Implementation

The proposed model is implemented in terms of a Fortran subroutine for the commercial finite element software Abaqus 2023 (Dassault Systèmes, 2023). Based on the model structure shown in Fig. 1, it would be possible to solve the thermal–metallurgical–chemical subproblem for all time steps, and to subsequently solve the mechanical problem. However, a fully coupled solution procedure is preferred in the implementation. This decision was made to simplify future additions to the model, which might introduce additional couplings, such as transformation plasticity. Implicit time integration was chosen due to the large time periods required for cooling to ambient temperature. Based on the choice of a time-implicit, thermo-mechanically coupled procedure, the model was implemented in Abaqus in terms of the Fortran user subroutines UMAT and UMATHT, which represent the mechanical and thermal material models at the quadrature point level.

3.1. Program structure

Every time an evaluation of the material model is required, Abaqus first calls the UMAT and subsequently the UMATHT subroutine. The implementation of a user material in the UMAT subroutine for a thermo-mechanically coupled problem requires the specification of the Cauchy stresses in Voigt notation $\boldsymbol{\sigma}_V$, the mechanical volumetric heat generation rate r_{pl}, and the updated internal variables $\boldsymbol{s}$ at the end of the time increment. Furthermore, the sensitivities of the stresses and heat generation rate with respect to the strain increment in Voigt notation $\Delta\boldsymbol{\varepsilon}_V$ and the temperature T are required. In the following, the symbol $\boldsymbol{s}$ refers to the actual array stored by Abaqus for each integration point, while the symbol $\boldsymbol{\kappa}$ will denote the set of internal variables required to describe the current microstructure. The vector $\boldsymbol{s}$ includes $\boldsymbol{\kappa}$, but also additional quantities for post processing, as shown in Table 3. During the call of the UMATHT subroutine, the internal thermal energy u and the heat flux vector $\boldsymbol{q}$ must be set, and the state variables $\boldsymbol{s}$ can optionally be updated again. For both internal thermal energy and heat flux, the sensitivities with respect to the temperature T and the temperature gradient ∇T are required. Finally, a variable denoted $p_{\Delta t}$ can be set in both subroutines to suggest the size of the next time increment if the automatic time step control is active. All output variables to be defined in the UMAT and UMATHT subroutines are listed in Table 4.

Taking into account the dependencies on the internal variables $\boldsymbol{\kappa}$, the sensitivities read

$$\frac{d\Delta\boldsymbol{\sigma}_V}{d\Delta\boldsymbol{\varepsilon}_V} = \frac{\partial\Delta\boldsymbol{\sigma}_V}{\partial\Delta\boldsymbol{\varepsilon}_V} + \frac{\partial\Delta\boldsymbol{\sigma}_V}{\partial\boldsymbol{\kappa}} \cdot \frac{d\boldsymbol{\kappa}}{d\Delta\boldsymbol{\varepsilon}_V}\,, \tag{54}$$

$$\frac{d\Delta\boldsymbol{\sigma}_V}{dT} = \frac{\partial\Delta\boldsymbol{\sigma}_V}{\partial T} + \frac{\partial\Delta\boldsymbol{\sigma}_V}{\partial\boldsymbol{\kappa}} \cdot \frac{d\boldsymbol{\kappa}}{dT}\,, \tag{55}$$

$$\frac{dr_{pl}}{d\Delta\boldsymbol{\varepsilon}_V} = \frac{\partial r_{pl}}{\partial\Delta\boldsymbol{\varepsilon}_V} + \frac{\partial r_{pl}}{\partial\boldsymbol{\kappa}} \cdot \frac{d\boldsymbol{\kappa}}{d\Delta\boldsymbol{\varepsilon}_V}\,, \tag{56}$$

$$\frac{dr_{pl}}{dT} = \frac{\partial r_{pl}}{\partial T} + \frac{\partial r_{pl}}{\partial\boldsymbol{\kappa}} \cdot \frac{d\boldsymbol{\kappa}}{dT}\,. \tag{57}$$

A residual equation of the format

$$\boldsymbol{R}_{\boldsymbol{\kappa}}(\boldsymbol{\kappa}) = \boldsymbol{0} \tag{58}$$

will be solved to obtain the internal variables $\boldsymbol{\kappa}$, where $\boldsymbol{\kappa}$ and $\boldsymbol{R}_{\boldsymbol{\kappa}}$ are specified in Section 3.3. Based on Eq. (58), the implicit function

Table 4
Output variables to be defined in the user material subroutines UMAT and UMATHT.

Variable name	Symbol	Description	Subroutine
STRESS	$\boldsymbol{\sigma_V}$	(Cauchy) stress tensor (Voigt notation)	UMAT
STAVEV	$\boldsymbol{s}$	Vector of state variables (see Table 3)	UMAT, UMATHT
RPL	r_{pl}	Mechanical heat generation per volume and unit time	UMAT
DDSDDE	$\frac{\mathrm{d}\Delta\boldsymbol{\sigma_V}}{\mathrm{d}\Delta\boldsymbol{\varepsilon}_V}$	Sensitivity of stress increments w.r.t. strain increments	UMAT
DDSDDT	$\frac{\mathrm{d}\boldsymbol{\sigma_V}}{\mathrm{d}T}$	Sensitivity of stress increments w.r.t. temperature	UMAT
DRPLDE	$\frac{\mathrm{d}r_{pl}}{\mathrm{d}\Delta\boldsymbol{\varepsilon}_V}$	Sensitivity of heat generation w.r.t. strain increments	UMAT
DRPLDT	$\frac{\mathrm{d}r_{pl}}{\mathrm{d}T}$	Sensitivity of heat generation w.r.t. temperature	UMAT
U	u	Internal thermal energy per unit mass	UMATHT
DUDT	$\frac{\mathrm{d}u}{\mathrm{d}T}$	Sensitivity of u w.r.t. temperature	UMATHT
DUDG	$\frac{\mathrm{d}u}{\mathrm{d}\nabla T}$	Sensitivity of u w.r.t. temperature gradient	UMATHT
FLUX	$\boldsymbol{q}$	Heat flux vector	UMATHT
DFDT	$\frac{\mathrm{d}\boldsymbol{q}}{\mathrm{d}T}$	Sensitivity of heat flux w.r.t. temperature	UMATHT
DFDG	$\frac{\mathrm{d}\boldsymbol{q}}{\mathrm{d}\nabla T}$	Sensitivity of heat flux w.r.t. temperature gradient	UMATHT
PNEWDT	$p_{\Delta t}$	Time increment ratio for automatic time stepping	UMAT, UMATHT

theorem is applied to determine the derivatives

$$\frac{\mathrm{d}\boldsymbol{\kappa}}{\mathrm{d}\Delta\boldsymbol{\varepsilon}_V} = -\left[\frac{\partial \boldsymbol{R}_{\boldsymbol{\kappa}}}{\partial \boldsymbol{\kappa}}\right]^{-1} \cdot \frac{\partial \boldsymbol{R}_{\boldsymbol{\kappa}}}{\partial \Delta\boldsymbol{\varepsilon}_V} = \boldsymbol{0}\,, \tag{59}$$

$$\frac{\mathrm{d}\boldsymbol{\kappa}}{\mathrm{d}T} = -\left[\frac{\partial \boldsymbol{R}_{\boldsymbol{\kappa}}}{\partial \boldsymbol{\kappa}}\right]^{-1} \cdot \frac{\partial \boldsymbol{R}_{\boldsymbol{\kappa}}}{\partial T}\,, \tag{60}$$

where the local Jacobian $\partial \boldsymbol{R}_{\boldsymbol{\kappa}}/\partial \boldsymbol{\kappa}$ was already computed to solve the system of evolution equations. It was already exploited in Eq. (59) that $\partial \boldsymbol{R}_{\boldsymbol{\kappa}}/\partial \Delta\boldsymbol{\varepsilon}_V = \boldsymbol{0}$ can be directly inferred from the coupling structure presented in Fig. 1. The required derivatives of the local residual $\boldsymbol{R}_{\boldsymbol{\kappa}}$ are specified in Appendix A.2, the derivatives of the stress increment $\Delta\boldsymbol{\sigma_V}$ in Appendix A.3, and the derivatives of the heat generation rate r_{pl} in Appendix A.4.

A graphical overview of the data flow in the subroutine structure is shown in Fig. 4, while the abstract steps in each of the subroutines are summarised in algorithms 1 and 2.

3.2. Regularised heaviside function

The activation functions for the phase transformations, i.e. ζ_{M} and ζ_{B}, are based on the Heaviside function H, which is non-continuous and therefore may cause convergence problems when the evolution equations are solved numerically. These problems are avoided by applying the approximation

$$\mathrm{H}(T) \approx \widetilde{\mathrm{H}} = \frac{1}{2}\left[\tanh(l\,T) + 1\right]\,, \tag{61}$$

where the parameter l governs the range over which the step function is regularised, and is chosen so that

$$\widetilde{\mathrm{H}}\left(T - 2\,^{\circ}\mathrm{C}\right) = 1\%\,, \quad \widetilde{\mathrm{H}}\left(T + 2\,^{\circ}\mathrm{C}\right) = 99\%\,. \tag{62}$$

The Heaviside function $\mathrm{H}\left(\dot{T}\right)$ in Eq. (32) is implemented as an if-condition to avoid any martensite evolution during heating.

3.3. Solution of evolution equations

At any quadrature point in a finite element simulation, the local balance Eqs. (5) and (8), as well as the evolution Eqs. (33) and (43) for the volume fractions must be solved. Using the mass balance (5), the austenite volume fraction can be expressed as

$$\beta_{\mathrm{A}} = 1 - \beta_{\mathrm{M}} - \beta_{\mathrm{B}}\,. \tag{63}$$

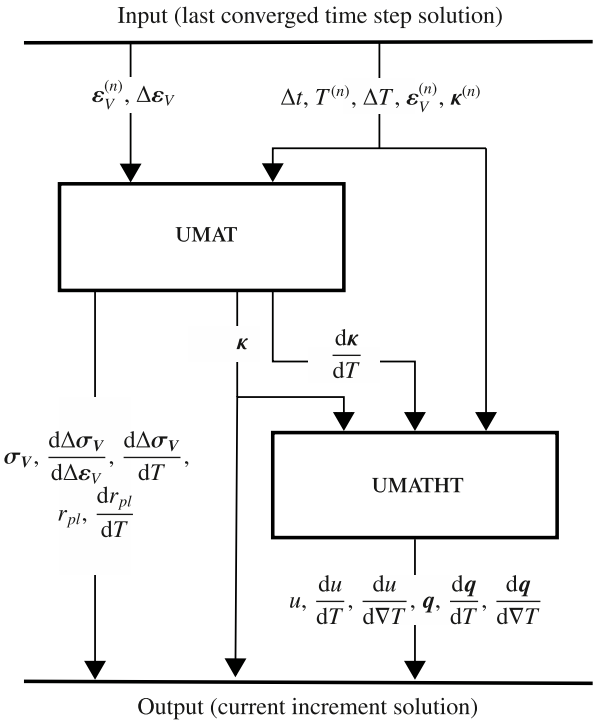

Fig. 4. Data flow during the call of the user subroutines UMAT and UMATHT. Both $\boldsymbol{\kappa}$ and $\mathrm{d}\boldsymbol{\kappa}/\mathrm{d}T$ are passed from UMAT to UMATHT in the vector of state variables $\boldsymbol{s}$.

The remaining internal variables at the quadrature point level are

$$\boldsymbol{\kappa} = \left[\beta_{\mathrm{M}}, \beta_{\mathrm{B}}, x_{\mathrm{C,A}}\right]^{\mathrm{t}}\,. \tag{64}$$

Restating Eq. (29), (33) and (38) in the rate form $\dot{\boldsymbol{\kappa}} = \boldsymbol{f}(\boldsymbol{\kappa})$ and introducing the abbreviation

$$A = \ln\left(\frac{\hat{\beta}_{\mathrm{B}}}{\hat{\beta}_{\mathrm{B}} - \beta_{\mathrm{B}}}\right) \tag{65}$$

Algorithm 1: Structure of user subroutine UMAT. Terms which vanish for the proposed model are neglected here.

Input: Δt, $T^{(n)}$, ΔT, $\boldsymbol{\varepsilon}_V^{(n)}$, $\Delta\boldsymbol{\varepsilon}_V$, $\boldsymbol{\sigma}_V^{(n)}$, $\boldsymbol{s}^{(n)}$

extract $\boldsymbol{\kappa}^{(n)}$ from $\boldsymbol{s}^{(n)}$

Step 1: Evolution equations for $\boldsymbol{\kappa}$ and derivatives

Calculate $\boldsymbol{\kappa}$ so that $\boldsymbol{R}_{\boldsymbol{\kappa}} = \boldsymbol{0}$

Calculate partial derivatives $\frac{\partial \boldsymbol{R}_{\boldsymbol{\kappa}}}{\partial \boldsymbol{\kappa}}$, $\frac{\partial \boldsymbol{R}_{\boldsymbol{\kappa}}}{\partial T}$

Apply implicit function theorem $\frac{\mathrm{d}\boldsymbol{\kappa}}{\mathrm{d}T} = -\left[\frac{\partial \boldsymbol{R}_{\boldsymbol{\kappa}}}{\partial \boldsymbol{\kappa}}\right]^{-1} \cdot \frac{\partial \boldsymbol{R}_{\boldsymbol{\kappa}}}{\partial T}$

Step 2: Constitutive model and derivatives

Calculate stresses $\boldsymbol{\sigma}_V$

Calculate partial derivatives $\frac{\partial \Delta\boldsymbol{\sigma}_V}{\partial \Delta\boldsymbol{\varepsilon}_V}$, $\frac{\partial \Delta\boldsymbol{\sigma}_V}{\partial T}$, $\frac{\partial \Delta\boldsymbol{\sigma}_V}{\partial \boldsymbol{\kappa}}$

Calculate rate of heat generation r_{pl}

Calculate partial derivatives $\frac{\partial r_{pl}}{\partial T}$, $\frac{\partial r_{pl}}{\partial \boldsymbol{\kappa}}$

Step 3: Sensitivities

$\frac{\mathrm{d}(\bullet)}{\mathrm{d}\Delta\boldsymbol{\varepsilon}_V} = \frac{\partial(\bullet)}{\partial \Delta\boldsymbol{\varepsilon}_V}$

$\frac{\mathrm{d}(\bullet)}{\mathrm{d}T} = \frac{\partial(\bullet)}{\partial T} + \frac{\partial(\bullet)}{\partial \boldsymbol{\kappa}} \cdot \frac{\mathrm{d}\boldsymbol{\kappa}}{\mathrm{d}T}$

Update $\boldsymbol{s}$ based on $\boldsymbol{\kappa}$ and $\mathrm{d}\boldsymbol{\kappa}/\mathrm{d}T$

Output: $\boldsymbol{\sigma}_V$, $\frac{\mathrm{d}\Delta\boldsymbol{\sigma}_V}{\mathrm{d}\Delta\boldsymbol{\varepsilon}_V}$, $\frac{\mathrm{d}\Delta\boldsymbol{\sigma}_V}{\mathrm{d}T}$, r_{pl}, $\frac{\mathrm{d}r_{pl}}{\mathrm{d}T}$, $\boldsymbol{s}$

Algorithm 2: Structure of user subroutine UMATHT. Terms which vanish for the proposed model are neglected here. The derivatives $\partial u/\partial\boldsymbol{\kappa}$ and $\partial \boldsymbol{q}/\partial\boldsymbol{\kappa}$ arise from phase-dependent material parameters.

Input: Δt, $T^{(n)}$, ΔT, $u^{(n)}$, $\boldsymbol{q}^{(n)}$, $\boldsymbol{s}^{(n)}$

extract $\boldsymbol{\kappa}^{(n)}$, $\boldsymbol{\kappa}$, and $\frac{\mathrm{d}\boldsymbol{\kappa}}{\mathrm{d}T}$ from $\boldsymbol{s}^{(n)}$

Step 1: Solve energy balance

Update internal thermal energy u

Calculate partial derivatives $\frac{\partial u}{\partial T}$, $\frac{\partial u}{\partial \nabla T}$, $\frac{\partial u}{\partial \boldsymbol{\kappa}}$

Step 2: Evaluate thermal constitutive law

Calculate heat flux $\boldsymbol{q}$

Calculate partial derivatives $\frac{\partial \boldsymbol{q}}{\partial T}$, $\frac{\partial \boldsymbol{q}}{\partial \nabla T}$, $\frac{\partial \boldsymbol{q}}{\partial \boldsymbol{\kappa}}$

Step 3: Compute Sensitivities

$\frac{\mathrm{d}(\bullet)}{\mathrm{d}T} = \frac{\partial(\bullet)}{\partial T} + \frac{\partial(\bullet)}{\partial \boldsymbol{\kappa}} \cdot \frac{\mathrm{d}\boldsymbol{\kappa}}{\mathrm{d}T}$

$\frac{\mathrm{d}(\bullet)}{\mathrm{d}\nabla T} = \frac{\partial(\bullet)}{\partial \nabla T}$

Output: u, $\frac{\mathrm{d}u}{\mathrm{d}T}$, $\frac{\mathrm{d}u}{\mathrm{d}\nabla T}$, $\boldsymbol{q}$, $\frac{\mathrm{d}\boldsymbol{q}}{\mathrm{d}T}$, $\frac{\mathrm{d}\boldsymbol{q}}{\mathrm{d}\nabla T}$

leads to the coupled system of evolution equations

$$\dot{\beta}_\mathrm{M} = -\zeta_\mathrm{M}\left[1-\beta_\mathrm{M}-\beta_\mathrm{B}\right] k\,\dot{T}\ , \tag{66a}$$

$$\dot{\beta}_\mathrm{B} = \begin{cases} 0.01\,\zeta_\mathrm{B}/\tau & \text{if } \beta_\mathrm{B} \le 1\% \\ \zeta_\mathrm{B} N\, b^{\frac{1}{N}}\left[\hat{\beta}_\mathrm{B}-\beta_\mathrm{B}\right] A^{\frac{N-1}{N}} & \text{if } \beta_\mathrm{B} > 1\% \end{cases}\ , \tag{66b}$$

$$\dot{x}_{\mathrm{C,A}} = \frac{\dot{\beta}_\mathrm{B}}{1-\beta_\mathrm{M}-\beta_\mathrm{B}}\left[x_{\mathrm{C,A}}-x_{\mathrm{C,B}}\right]\ . \tag{66c}$$

Inserting Eq. (66b) into Eq. (66c) yields the desired format, but is omitted here for readability.

Starting from increment n at time $t^{(n)}$, with known values $\boldsymbol{\kappa}^{(n)}$ and $T^{(n)}$, a time step $\Delta t = t^{(n+1)} - t^{(n)}$ to the next time increment $n+1$ is considered. The temperature $T^{(n+1)}$ is known at the material point level, but has to be taken into consideration when deriving the consistent tangent. Time discretisation is performed based on the implicit Euler integration scheme, i.e.

$$\dot{\boldsymbol{\kappa}} \approx \frac{\boldsymbol{\kappa}^{(n+1)} - \boldsymbol{\kappa}^{(n)}}{\Delta t}\ . \tag{67}$$

In the following the superscript $*^{(n+1)}$ will be omitted to improve readability. Applying the time discretisation to Eq. (66) yields the discrete residual equation

$$\boldsymbol{R}_{\boldsymbol{\kappa}} = \left[R_{\beta_\mathrm{M}}\ R_{\beta_\mathrm{B}}\ R_{x_{\mathrm{C,A}}}\right]^\mathrm{t} = \boldsymbol{0} \tag{68}$$

with

$$R_{\beta_\mathrm{M}} = \beta_\mathrm{M} - \beta_\mathrm{M}^{(n)} + \zeta_\mathrm{M}\left[1-\beta_\mathrm{M}-\beta_\mathrm{B}\right] k\Delta T\ , \tag{69a}$$

$$R_{\beta_\mathrm{B}} = \begin{cases} \beta_\mathrm{B} - \beta_\mathrm{B}^{(n)} - 0.01\,\zeta_\mathrm{B}\,\Delta t/\tau & \text{if } \beta_\mathrm{B}^{(n)} \le 1\% \\ \beta_\mathrm{B} - \beta_\mathrm{B}^{(n)} - \Delta t\zeta_\mathrm{B} N\, b^{\frac{1}{N}}\left[\hat{\beta}_\mathrm{B}-\beta_\mathrm{B}\right] A^{\frac{N-1}{N}} & \text{if } \beta_\mathrm{B}^{(n)} > 1\% \end{cases}\ , \tag{69b}$$

$$R_{x_{\mathrm{C,A}}} = \left[1-\beta_\mathrm{M}-\beta_\mathrm{B}\right]\left[x_{\mathrm{C,A}} - x_{\mathrm{C,A}}^{(n)}\right] - \left[\beta_\mathrm{B}-\beta_\mathrm{B}^{(n)}\right]\left[x_{\mathrm{C,A}} - x_{\mathrm{C,B}}\right]\ . \tag{69c}$$

Switching between nucleation and further evolution in Eq. (69b) is implemented based on the last converged time step to improve numerical stability. A trust-region algorithm, provided in the Fortran version of the Intel MKL library, is used to solve the nonlinear equation Eq. (68). The required Jacobian $\partial \boldsymbol{R}_{\boldsymbol{\kappa}}/\partial\boldsymbol{\kappa}$ is provided in Appendix A.2.

3.4. Stress update

The time-discrete stress increment $\Delta\boldsymbol{\sigma}_V$ is obtained in a straightforward manner from Eq. (14) as

$$\Delta\boldsymbol{\sigma}_V = \mathbf{E}_V \cdot \left[\left[\boldsymbol{\varepsilon}_V^{\mathrm{el}}\right]^{(n)} + \Delta\boldsymbol{\varepsilon}_V^{\mathrm{el}}\right] - \boldsymbol{\sigma}_V^{(n)}\ , \tag{70}$$

where the elastic strain increment reads

$$\Delta\boldsymbol{\varepsilon}_V^{\mathrm{el}} = \Delta\boldsymbol{\varepsilon}_V - \alpha\,\Delta T\,\boldsymbol{I}_V - \Delta\gamma\,\boldsymbol{I}_V \tag{71}$$

with the second-order identity tensor in Voigt notation $\boldsymbol{I}_V$. By using Eqs. (16) and (17), the elasticity tensor in Voigt notation can be computed as

$$\mathbf{E}_V = \sum_i \beta_i\,\mathbf{E}_{i,V}\ , \tag{72}$$

where the elasticity tensor $\mathbf{E}_{i,V}$ for each individual phase is computed following Eq. (15), and the thermal expansion coefficient reads

$$\alpha = \sum_i \beta_i\,\alpha_i\ . \tag{73}$$

The discrete increment of the linear transformation strain is given by

$$\Delta\gamma = \sum_i \Delta\beta_i\,\gamma_i\ , \tag{74}$$

where $\Delta\beta_i$ denotes the increment in the respective volume fraction. Derivatives required for the FE implementation are specified in Appendix A.3.

3.5. Heat generation rate

The only part of the model contributing to the mechanical heat generation rate is the latent heat of the transformations, given by Eq. (53), which is approximated as

$$r_{pl} = \frac{\beta_\mathrm{M} - \beta_\mathrm{M}^{(n)}}{\Delta t}\,\rho\,\Delta h_{\mathrm{A}\to\mathrm{M}} + \frac{\beta_\mathrm{B} - \beta_\mathrm{B}^{(n)}}{\Delta t}\,\rho\,\Delta h_{\mathrm{A}\to\mathrm{B}}\ . \tag{75}$$

Derivatives for the FE implementation are given in Appendix A.4.

4. Representative simulation results

Representative finite element simulations have been performed to demonstrate the application of the proposed model. To demonstrate the coupling during the incomplete bainite transformation, a homogeneous, quasi-isothermal demonstration case above the martensite start

Table 5
Consistent mm-g-ms unit system, including units of selected derived quantities.

Quantity	Length	Mass	Time	Density	Force	Stress	Energy	Power
Unit	mm	g	ms	g mm^{-3}	N	MPa	mJ	W

temperature M_S is considered in Section 4.2. Coupled evolution of martensite and bainite during cooling is considered in Section 4.3 for a homogeneous problem, and in Section 4.4 for the quenching of a complex axisymmetric workpiece.

All simulations presented in this work have been performed in the mm-g-ms unit system presented in Table 5.

4.1. Choice of model parameters

All remaining model parameter choices for the representative simulations are summarised in this section. Table 6 gives an overview of all material parameters, except those for the phase transformation models, as functions of temperature T where applicable. Values for Young's modulus, Poisson's ratio, thermal expansion coefficient, specific heat capacity and thermal conductivity were published in Mustak et al. (2016) for different phases of 100Cr6 and are adopted in this work for both material grades. As no specific values were available for 100Cr or 100CrMnSi6-4, the transformation strains and latent heat of transformation are chosen based on the values proposed in Denis et al. (1985, 1987) for 60NCD11 and XC80 steels. The overall mass density was approximated from general values for steel, since the differences between the phases are not considered as model parameters. It was assumed that carbide-free bainite with carbon content $x_{C,B} = 0.03\%$ forms in 100CrMnSi6-4, while the bainite phase carbon content was assumed to be $x_{C,B} = x_C = 1.00\%$ in 100Cr6. This assumption was made to demonstrate the model capabilities and the interaction of the evolution of the carbon content, and is not generally fulfilled.

To obtain the polynomial coefficients $\boldsymbol{p}$ for the temperature dependent JMAK model, see Eq. (48), the optimisation described in Section 2.7 was performed based on a TTT-diagram published in Kaymak (2007). Table 7 lists the optimal set of parameters $\boldsymbol{p}^*$. A comparison of the input data with the model prediction for the isothermal bainite transformation is presented in Fig. 5 and shows good agreement between the model and the input data. Only the bainite transformation model is verified here, since the JMAK parameters were obtained from an optimisation procedure based on a TTT diagram rather than from the literature or from MatCalc, and are therefore more prone to errors.

Following Gür and Tekkaya (2001), the heat transfer coefficient for the quenching in water with a sink temperature of 20 °C and 60 °C is linearly interpolated from the values presented in Table 8.

4.2. Bainite evolution under homogeneous, constant ambient temperature

A homogeneous state of deformation, temperature, and microstructure is considered in three-dimensional simulations of a cube with an edge length of 1 mm. Constant ambient temperature conditions are assumed for this demonstration case, and are implemented either in terms of Dirichlet-type boundary conditions on all temperature degrees of freedom, or as convection boundary conditions on all faces of the cube. The initial temperature as well as the ambient temperature are chosen as 300 °C for this case, and the heat transfer coefficient is assumed to be constant at $h = 1\,\mathrm{e}{-4}\,\mathrm{W\,mm^{-2}\,°C^{-1}}$. A fully austenitic initial microstructure is assumed, and no martensite evolution takes place since this temperature is above the martensite start temperature M_S. Fig. 6 shows selected results for a total time span of 500 s.

Given enough time, the model predicts a final microstructure that is nearly 100% bainitic for 100Cr6, where the implementation of the thermal conditions has a noticeable impact on the transformation rate. The Dirichlet-constraint problem assumes that the latent heat is immediately transported to the surrounding medium, while the retarded

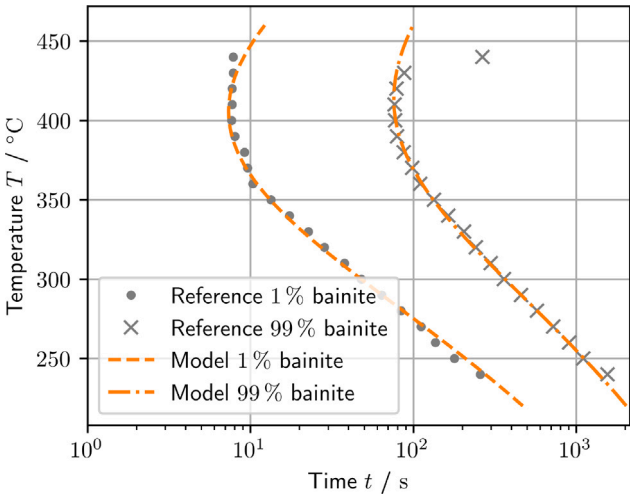

Fig. 5. Comparison of input data and model prediction for the isothermal transformation from austenite to bainite. Grey markers represent points extracted from the TTT–diagram published in Kaymak (2007), while orange lines show model prediction of transformation onset and finish after identification of polynomial parameters $\boldsymbol{p}^*$ for the temperature-dependent JMAK model.

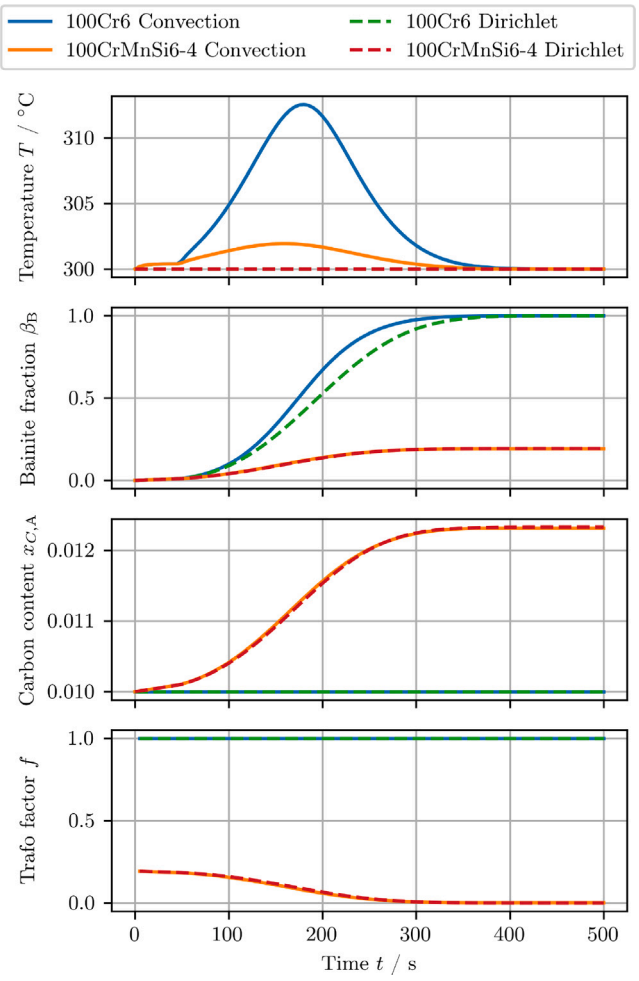

Fig. 6. Homogeneous evolution of temperature T, bainite volume fraction β_B, austenite phase carbon content $x_{C,A}$, and incomplete bainite transformation function f, under constant ambient temperature of 300 °C. Both implementations of the thermal conditions are shown.

Table 6
Mechanical and thermal model parameters for each phase, based on (1) Mustak et al. (2016), (2) Denis et al. (1985), (3) Denis et al. (1987). All temperature-dependent expressions are given in terms of the dimensionless temperature $\tilde{T} = T/°C$.

Parameter	Symbol	Value	Unit	Source
Mass density	ρ	0.00785	g mm^{-3}	
Young's modulus	E_A	204 000.0−91.0 × $\tilde{T}$	MPa	1
	E_M, E_B	212 000.0−52.7 × $\tilde{T}$	MPa	1
Poisson's ratio	ν_A	0.223 + 0.00025 × $\tilde{T}$	–	1
	ν_M, ν_B	0.344 + 0.00010 × $\tilde{T}$	–	1
Thermal expansion coefficient	α_A	22.2 e−6	°C^{-1}	1
	α_M , α_B	11.7 e−6	°C^{-1}	1
Transformation strain	γ_A	0	–	
	γ_M	1.11 e−2	–	2
	γ_B	5.0 e−3	–	3
Specific heat capacity	$c_{p,A}$	448.67 + 0.3007 × $\tilde{T}$ − 2.49 e−4 × $\tilde{T}^2$ + 1.42 e−7 × $\tilde{T}^3$	mJ g^{-1} °C^{-1}	1
	$c_{p,M}$, $c_{p,B}$	336.51 + 0.4875 × $\tilde{T}$ − 6.16 e−4 × $\tilde{T}^2$ + 1.62 e−6 × $\tilde{T}^3$	mJ g^{-1} °C^{-1}	1
Thermal conductivity	Λ_A	1.68 e−2 + 1.19 e−5 × $\tilde{T}$	W mm^{-1} °C^{-1}	1
	Λ_M, Λ_B	3.93 e−2 + 2.4 e−5 × $\tilde{T}$ − 6.43 e−8 × $\tilde{T}^2$	W mm^{-1} °C^{-1}	1
Latent heat	$\rho\,\Delta h_{A\to M}$	6.4 e2	mJ mm^{-3}	2
	$\rho\,\Delta h_{A\to B}$	1.56 e3 − 1.5 × $\tilde{T}$	mJ mm^{-3}	3

Table 7
Optimal parameters p^* for the temperature-dependent JMAK model parameters $b_p(T)$ and $N_p(T)$ in Eq. (48), based on least squares fit to the TTT–diagram published in Kaymak (2007).

$p^*_{b,0}$	$p^*_{b,1}$/°C^{-1}	$p^*_{b,2}$/°C^{-2}	$p^*_{N,0}$	$p^*_{N,1}$/°C^{-1}	$p^*_{N,2}$/°C^{-2}
−1.8847 e2	8.1383 e−1	−1.0303 e−3	1.1313 e1	−4.5363 e−2	5.8965 e−5

Table 8
Heat transfer coefficient $h(T)$ for quenching in water at 20 °C and 60 °C taken from Gür and Tekkaya (2001).

T_∞/°C	h_c/W mm^{-2} °C^{-1}	
	T = 20 °C	T = 60 °C
0	0.00435	0.0001353
200	0.0082071	0.0020292
400	0.0119617	0.0028409
430	0.0134917	–
445	–	0.0032912
500	0.0125	0.003422
560	0.0102062	–
570	–	0.0026109
600	0.007793	0.002157
700	0.002507	–
800	0.0004371	0.0002302
900	0.0001352	0.0001352

transport of heat due to convection leads to a temporary temperature increase of approximately 12 °C during the initial stage of the transformation. Faster transformation times in the elevated temperature regime lead to a faster completion of the bainite transformation when compared to the Dirichlet-constraint problem. As expected, the austenite phase carbon concentration remains constant for 100Cr6.

For 100CrMnSi6-4, the expected austenite phase carbon content after the transformation can be obtained from Fig. 3 as $x_{C,A} \approx 1.25\%$, which is in good accordance with the simulation results. Compared to 100Cr6, the temperature increase in the case of convection boundary conditions is lower at approximately 2 °C, which is in accordance with the lower transformation rates and therefore lower release of latent heat. Due to the small temperature increase, the differences in the evolution of the bainite volume fraction and austenite phase carbon content due to the different implementations of thermal conditions are negligible for 100CrMnSi6-4.

4.3. Microstructure evolution during homogeneous cooling

As in Section 4.2, a homogeneous state is considered for the cube. From a fully austenitic initial microstructure and an initial temperature of 500 °C, convectional heat transfer with a transfer coefficient of h = 1 e−5 W mm^{-2} °C^{-1} to a surrounding medium at 60 °C is prescribed as the thermal boundary condition. The results for this example are presented in Fig. 7.

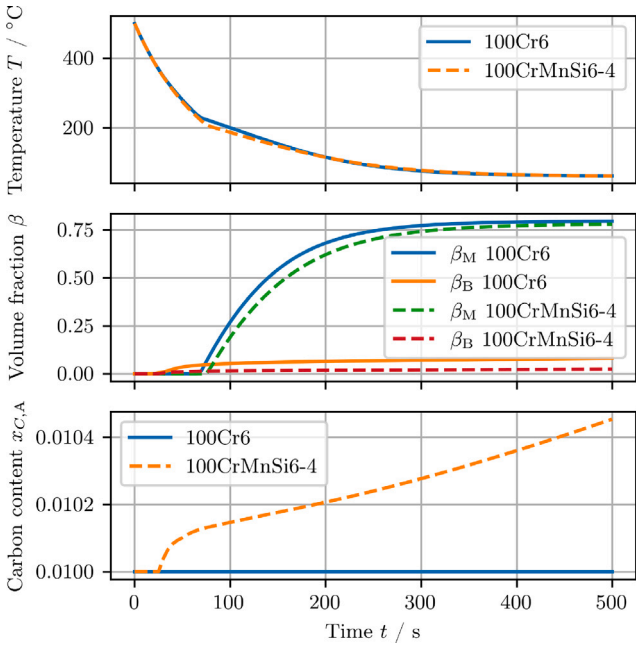

Fig. 7. Homogeneous evolution of temperature T, bainite volume fraction β_B, austenite phase carbon content $x_{C,A}$, and strain component ϵ_{11}, during cooling from 500 °C to 60 °C.

Three stages of transformation can be observed in the results: During the initial stage of approximately 20 s, no evolution of the microstructure takes place, until the temperature reaches the bainite start temperature B_S. During the second stage, the transformation to bainite begins, while the temperature continues to drop towards the martensite start temperature M_S, which is reached at approximately 75 s. The third stage of the transformation is characterised by a simultaneous transformation of austenite to bainite and martensite, with the phase fractions saturating towards the end of the simulation.

A final microstructure of approximately 79.5% martensite and 8% bainite is reached in the case of 100Cr6, while for 100CrMnSi6-4

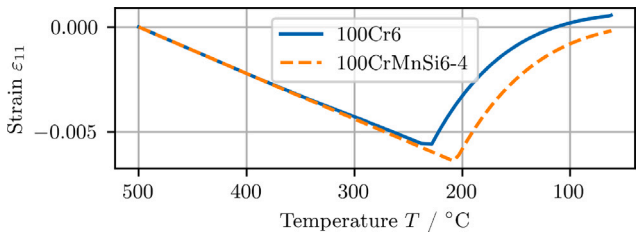

Fig. 8. Evolution of strain in normal direction during cooling from 500 °C to 60 °C.

a martensite fraction of 78% and a bainite fraction of 2.5% can be observed. In line with the predominant transformation to martensite, the temperature graph does not visibly change at the onset of the bainite transformation after stage one, while a kink can be observed at the beginning of stage three due to the latent heat release. Although the bainite transformation seems to be nearly complete after the simulation time of 500 s, the austenite phase carbon content $x_{C,A}$ still evolves at this point in time. However, a longer simulation showed the expected saturation after approximately 5000 s without significant further impact on the final microstructure. This behaviour can be explained by the longer timescale of the bainite transformation at lower temperatures, while only a small amount of austenite remains to transform due to the competing growth of the martensite phase.

The normal strain at each temperature is shown in Fig. 8. Since no external forces act on the cube, the resulting strain represents the addition of thermal strain and transformation strain. During the transformation-free initial stage, as expected due to the constant heat expansion coefficient, a linear correlation can be observed. The nonlinearity during the second stage, caused by the onset of bainite transformation and the corresponding transformation strain, is barely visible due to the low rate of transformation. However, the transformation strains during the third stage, dominated by the martensite transformation, are large enough to cause an expansion instead of further shrinkage.

4.4. Microstructure evolution during quenching of a complex workpiece

The quench hardening of the inner race of a tapered roller bearing is considered as an example for the application of the proposed model to an industrial use case. Bearing components represent a typical application of the materials considered in this work, and the varying cross-section facilitates the development of an inhomogeneous microstructure distribution in the workpiece. While the example problem is of academic nature and has been chosen to demonstrate the capabilities of the proposed model, an effort is made to approximate realistic process conditions based on the literature. Fine-tuning the model parameters to mirror a specific real process and validating the model, e.g. through measurements of temperature curves and microstructure distributions, is beyond the scope of this work due to the required effort.

A rendering of the bearing race is presented along with the cross-section in Fig. 9. Two element centroids, close to the centre points of the thinnest and thickest sections of the cross-section, are chosen as probing locations, denoted P_1 and P_2.

For all quenching simulations, a homogeneous initial microstructure of 100% austenite at an initial temperature of 850 °C is prescribed. Water at either $T_\infty = 20\,°C$ or $T_\infty = 60\,°C$ is considered as the cooling medium, and the temperature-dependent transfer coefficients for convectional heat transfer, as proposed in Gür and Tekkaya (2001), are presented in Table 8. Simulations have been performed for both, 100Cr6 and 100CrMnSi6-4 with both quenching bath temperatures.

Since the workpiece exhibits rotational symmetry, a structured mesh of 3802 axisymmetric quad elements of type CAX4T are used in Abaqus to reduce the computational cost. Rigid body motions are prevented

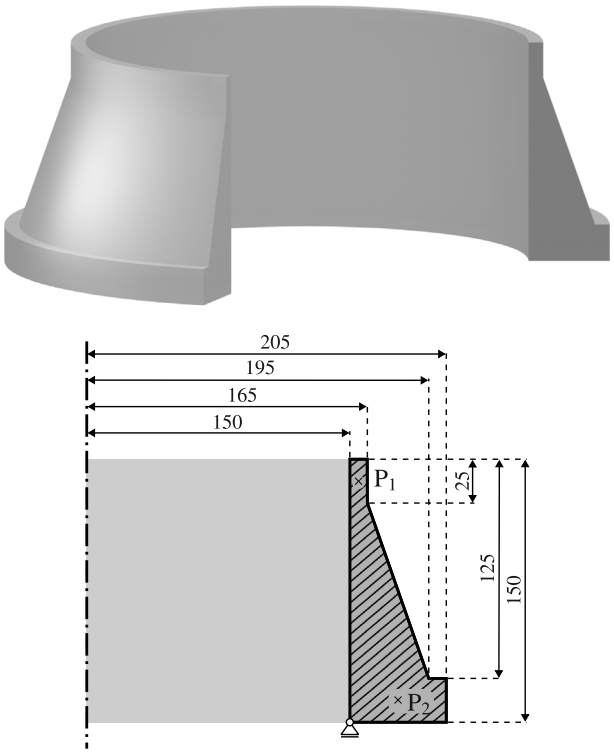

Fig. 9. Rendering and boundary value sketch of the bearing race. The 110° view cut reveals the cross-section, for which all dimensions are given in the sketch in mm. Time history will be shown for the locations marked in the sketch as P_1 and P_2.

by constraining displacements of a single node in z-direction. The quenching process is simulated for a total time interval of 11 min, after which the highest temperature in the workpiece deviates from the quenching bath temperature by less than 1.5 °C in all simulations.

Temperature, bainite fraction, martensite fraction and von Mises stresses at the end of the simulations are presented as contour plots over the deformed configuration of the workpiece cross-section in Figs. 10–13. These results are also available at https://github.com/InstituteOfMechanics/Phase_Trafos_Carbon_Repartitioning in the vtk file format, exported using the open source software Paraqus (Furlan et al., 2025).

It is clear from Fig. 10 that the temperature distribution is close to uniform at the end of the simulations. In the case of a quenching bath temperature of $T_\infty = 20\,°C$, the maximum temperature difference in the workpiece is below 0.1 °C for both materials, while the remaining temperature difference for $T_\infty = 260\,°C$ is approximately 1.2 °C for 100Cr6 and 0.7 °C for 100CrMnSi6-4. In all four cases, the warmer part of the workpiece is located towards the centre of gravity of the cross-section.

The variation of the martensite fraction throughout the workpiece is highest for the combination of $T_\infty = 60\,°C$ and 100Cr6 at approximately 4%. A variation of 1.7% is found for $T_\infty = 60\,°C$ and 100CrMnSi6-4, while the variation is below 1% for both materials when the quenching bath temperature is chosen as $T_\infty = 20\,°C$. The total value of the martensite fraction lies between approximately 80% and 90% for all simulations, where larger martensite fractions are achieved at $T_\infty = 20\,°C$. Accordingly, the bainite fraction at the end of the simulation is larger at $T_\infty = 60\,°C$, with approximately 5% for 100Cr6 and 1.5% for 100CrMnSi6-4, while at $T_\infty = 20\,°C$ the bainite fraction remains below 1% for both materials.

The predicted residual stresses reach between approximately 6 MPa and 16 MPa, depending on the material and quenching bath temperature. Although the absolute values are relatively low, the distribution

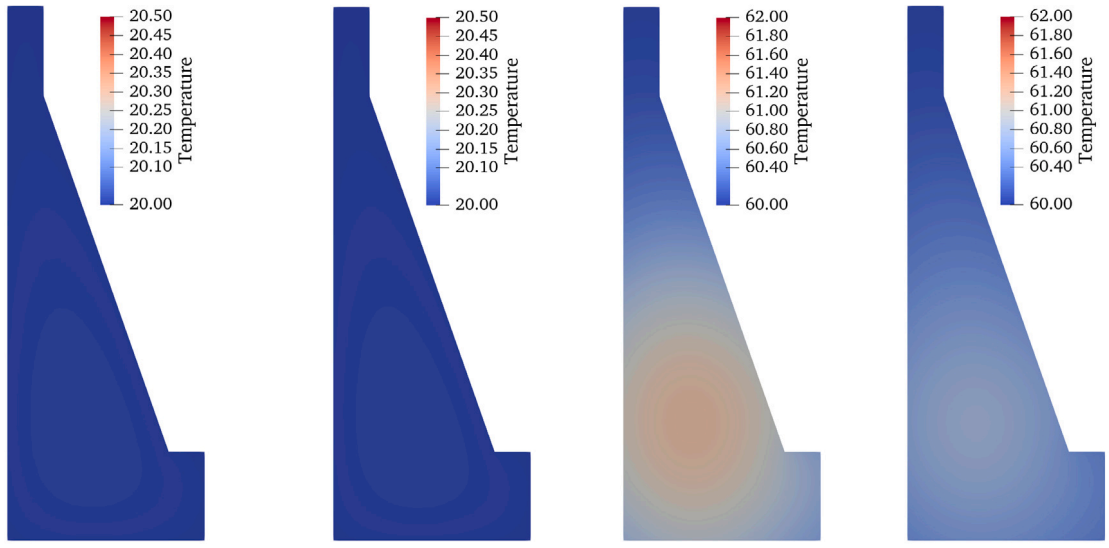

(a) 100Cr6, $T_\infty = 20\,°C$ (b) 100CrMnSi6-4, $T_\infty = 20\,°C$ (c) 100Cr6, $T_\infty = 60\,°C$ (d) 100CrMnSi6-4, $T_\infty = 60\,°C$

Fig. 10. Contour plot of temperature distribution at the end of the simulation.

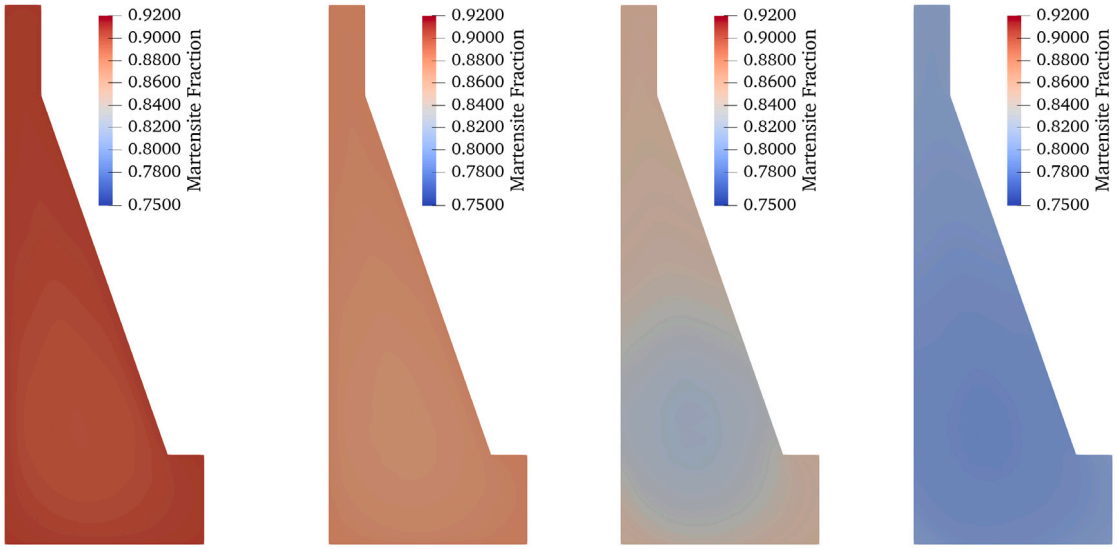

(a) 100Cr6, $T_\infty = 20\,°C$ (b) 100CrMnSi6-4, $T_\infty = 20\,°C$ (c) 100Cr6, $T_\infty = 60\,°C$ (d) 100CrMnSi6-4, $T_\infty = 60\,°C$

Fig. 11. Contour plot of the distribution of martensite fraction at the end of the simulation.

of the stresses within the workpiece is quite inhomogeneous. A typical quality measure for the heat treatment would be the achieved geometrical tolerances, especially of functional surfaces. The radial displacement over the length of the inner bore at the end of the simulation is shown in Fig. 14 in comparison for all four cases. It should be noted that residual stresses and distortion are presented for demonstration purposes, but, as discussed in Section 2.2, a model extension to include TRIP effects would be required to generate realistic results.

A slight conical shape of the inner bore can be observed for all four cases. However, lower absolute radial displacements as well as smaller displacement gradients along the bore length are predicted for 100Cr6 compared to 100CrMnSi6-4. Quenching at $T_\infty = 20\,°C$ yields lower radial displacements than at $T_\infty = 60\,°C$ for both material grades.

The evolution of temperature and microstructure at the two probing points during the first 180 s is shown in Figs. 15 and 16. While a faster cooling can be observed at the lower quenching bath temperature, the material choice has very little impact on the temperature history. At point P_1, a higher cooling rate is achieved compared to point P_2, which is due to the smaller cross-section.

In summary, the proposed model was successfully applied in a finite element simulation of a complex boundary value problem to predict phase transformations, including the interactions of the austenite phase carbon content with the transformation parameters. It was possible to determine the impact of the material choice as well as different quenching temperatures on the evolution of the microstructure as well as the resulting geometry after quenching.

5. Conclusion

The model proposed in this work combines the classic phenomenological KM and JMAK phase transformation models with a newly proposed coupling between the austenite phase carbon content and the phase fractions to include the effects of an evolving chemical composition

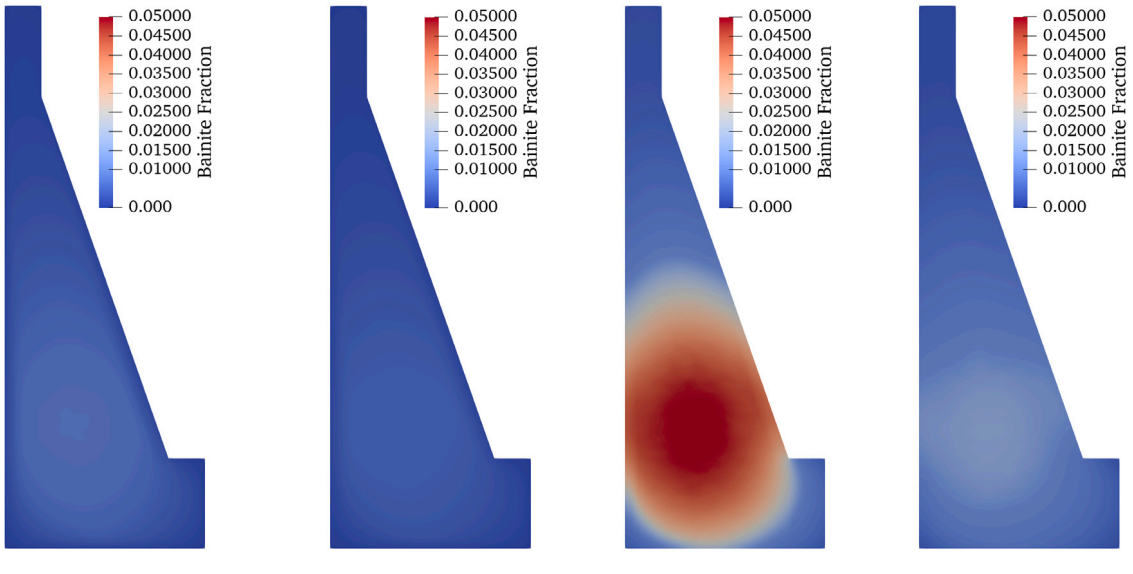

(a) 100Cr6, $T_\infty = 20\,^\circ\mathrm{C}$ (b) 100CrMnSi6-4, $T_\infty = 20\,^\circ\mathrm{C}$ (c) 100Cr6, $T_\infty = 60\,^\circ\mathrm{C}$ (d) 100CrMnSi6-4, $T_\infty = 60\,^\circ\mathrm{C}$

Fig. 12. Contour plot of the distribution of bainite fraction at the end of the simulation.

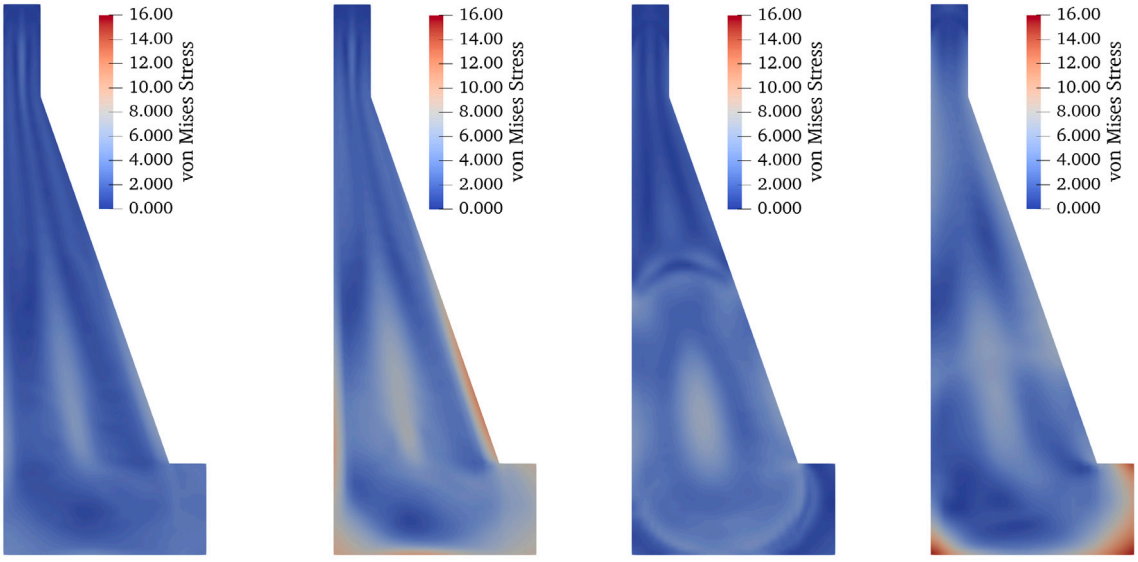

(a) 100Cr6, $T_\infty = 20\,^\circ\mathrm{C}$ (b) 100CrMnSi6-4, $T_\infty = 20\,^\circ\mathrm{C}$ (c) 100Cr6, $T_\infty = 60\,^\circ\mathrm{C}$ (d) 100CrMnSi6-4, $T_\infty = 60\,^\circ\mathrm{C}$

Fig. 13. Contour plot of von Mises stress distribution at the end of the simulation.

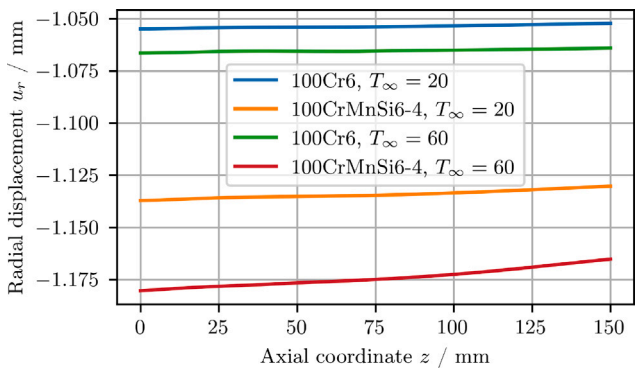

Fig. 14. Comparison of radial displacements along the inner bore length.

during incomplete formation of carbide-free bainite. An implementation of the model for the finite element software Abaqus, accessible at https://github.com/InstituteOfMechanics/Phase_Trafos_Carbon_Repartitioning, was successfully applied to simulate the quench hardening of a bearing component. It was demonstrated that the resulting microstructure can be predicted by the simulation for different process parameters.

A good calibration of all model components is crucial in order to obtain realistic predictions. For the presented examples, the calibration of the model was based on literature values, parameter fitting based on TTT–diagrams, and MatCalc simulations. The results clearly demonstrate that, for the application of the model to real-world problems, a detailed calibration and validation not only of the phase transformation models, but also of the model and boundary conditions for thermal conductance and heat transfer is crucial.

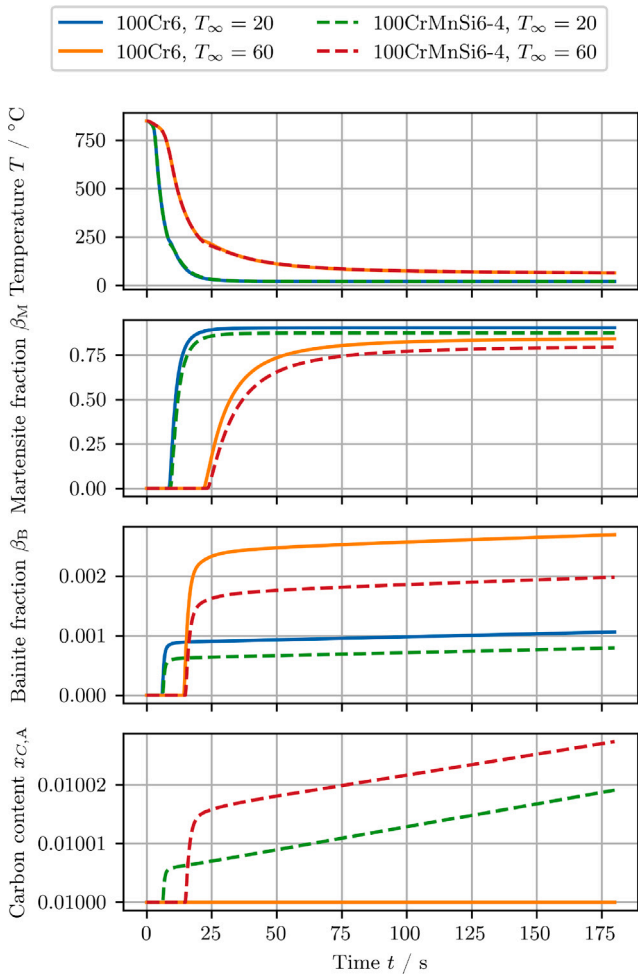

Fig. 15. Evolution of temperature and microstructure at point P_1 during the first 180 s of the simulations.

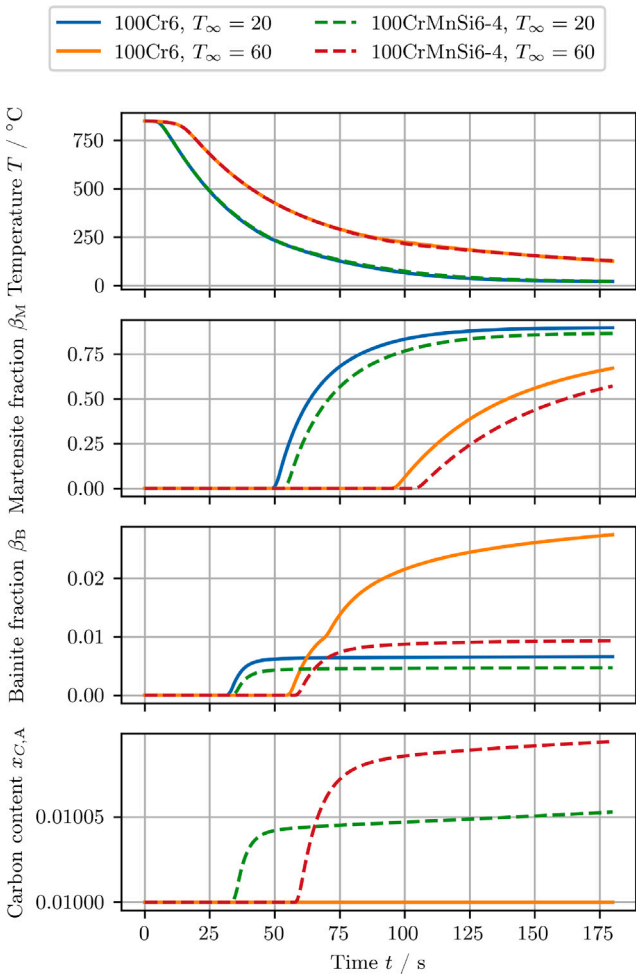

Fig. 16. Evolution of temperature and microstructure at point P_2 during the first 180 s of the simulations.

A possible improvement for future work is the application of more advanced models for the martensite and bainite transformations. Furthermore, the incorporation of plasticity and transformation-induced plasticity models is planned, which are considered essential for the prediction of realistic residual stresses and workpiece distortion. Another improvement for the realistic prediction of residual stresses is the implementation of alternative homogenisation methods, such as the Reuss-Sachs ansatz or more advanced relaxation approaches. Depending on the use case, the model could also be extended to incorporate the stress dependency of the transformations.

CRediT authorship contribution statement

Tim Furlan: Writing – original draft, Visualization, Software, Methodology, Investigation, Funding acquisition, Conceptualization, Writing – review & editing. **Markus Schewe:** Writing – review & editing, Methodology, Conceptualization. **Philipp Scherm:** Writing – review & editing, Software, Methodology, Investigation. **Philipp Retzl:** Writing – review & editing, Software, Methodology. **Ernst Kozeschnik:** Writing – review & editing, Supervision, Resources, Project administration, Funding acquisition, Conceptualization. **Andreas Menzel:** Writing – review & editing, Supervision, Resources, Project administration, Funding acquisition, Conceptualization.

Declaration of Generative AI and AI-assisted technologies in the writing process

During the preparation of this work the authors used chatGPT and deepL in order to improve the language of individual sections. After using this tool/service, the authors reviewed and edited the content as needed and take full responsibility for the content of the publication.

Funding

The research project “Produce to Performance” of the Research Association FGW (www.fgw.de) is supported by the BMWK, the AiF (grant Cornet 325 EN) and the DLR (grant 01IF00325C) as part of the program for promoting IGF based on a decision by the German Bundestag.

Partial financial support by the Deutsche Forschungsgemeinschaft (DFG, German Research Foundation) – Project-ID 278868966 – TRR 188 is gratefully acknowledged.

The authors would like to acknowledge the Austrian Research Promotion Agency (FFG) for the financial support related to the project No. FO999888200 “Produce to performance”.

Declaration of competing interest

The authors declare that they have no known competing financial interests or personal relationships that could have appeared to influence the work reported in this paper.

Acknowledgements

The authors would like to acknowledge the valuable discussions within the user committee of the Cornet Project Produce to Performance.

Appendix

A.1. Initial guess for the bainite transformation model parameter identification

As described in Section 2.7, the choice of initial guess for the nonlinear least squares fit presented in Eq. (50) is not trivial. Recall that the input data obtained from the TTT–diagram consists of m discrete temperatures T_i and the corresponding times $t_{1,i}$ and $t_{99,i}$ required for the formation of 1% and 99% martensite. Introducing constant parameters b_i and N_i, the JMAK model for the isothermal transformation at temperature T_i reads

$$\beta_{\mathrm{B},i}(t) = 1 - \exp\left(-b_i\, t^{N_i}\right) \,, \tag{A.1}$$

or, solved for t,

$$t(\beta_{\mathrm{B},i}) = \left[\frac{1}{b_i}\ln\left(\frac{1}{1-\beta_{\mathrm{B},i}}\right)\right]^{\frac{1}{N_i}} \,, \tag{A.2}$$

where b_i and N_i are determined for each temperature individually by the nonlinear optimisation

$$(\hat{b}_i, \hat{N}_i) = \arg\min_{b_i, N_i}\left\{\left[\beta_{\mathrm{B},i}(t_{1,i}) - 0.01\right]^2 + \left[\beta_{\mathrm{B},i}(t_{99,i}) - 0.99\right]^2\right\} \,. \tag{A.3}$$

It is remarked that, as shown in e.g. Tzitzelkov et al. (1974), in the isothermal case with only two lines in the diagram, a unique solution to Eq. (A.3) exists for each temperature, which will be denoted as the *isothermal fit* in the following. Inserting the isothermal solution into Eq. (A.2), and evaluating for $\beta_{\mathrm{B},i} = 1\%$ and $\beta_{\mathrm{B},i} = 99\%$, the data points in the input data are recovered up to numerical tolerances.

Given the discrete pairs $(T_i, \hat{b}_i)$ and $(T_i, \hat{N}_i)$, the polynomial ansatz

$$\ln\left(b_p(T)\right) = p_{b,0} + p_{b,1}\, T + p_{b,2} T^2 \,, \tag{A.4}$$

$$N_p(T) = p_{N,0} + p_{N,1} T + p_{N,2} T^2 \,, \tag{A.5}$$

is considered to approximate the temperature dependence of the parameters, and the vectors $\boldsymbol{p}_b = \left[p_{b,0},\, p_{b,1},\, p_{b,2}\right]^{\mathrm{t}}$ and $\boldsymbol{p}_N = \left[p_{N,0},\, p_{N,1},\, p_{N,2}\right]^{\mathrm{t}}$ are introduced. The least squares problems

$$\tilde{\boldsymbol{p}}_b = \arg\min_{\boldsymbol{p}_b}\left\{\sum_i^m \left[\log_{10}\left(b_p(T_i)\right) - \log_{10}\left(\hat{b}_i\right)\right]^2\right\} \,, \tag{A.6}$$

$$\tilde{\boldsymbol{p}}_N = \arg\min_{\boldsymbol{p}_N}\left\{\sum_i^m \left[N_p(T_i) - \hat{N}_i\right]^2\right\} \tag{A.7}$$

yield the optimal parameters $\tilde{\boldsymbol{p}}_b$ and $\tilde{\boldsymbol{p}}_N$ and the corresponding polynomials $\tilde{b}_p(T)$ and $\tilde{N}_p(T)$. The evaluation of the JMAK model based on these parameters will be denoted the *parameter fit* in the following.

The solution $\tilde{\boldsymbol{p}} = \left[\tilde{p}_{b,0},\, \tilde{p}_{b,1},\, \tilde{p}_{b,2},\, \tilde{p}_{N,0},\, \tilde{p}_{N,1},\, \tilde{p}_{N,2}\right]^{\mathrm{t}}$ is then used as the initial guess for the parameter identification based on the JMAK model, described in Section 2.7 and referred to as the *model fit* in the following, yielding the optimal set of parameters $\boldsymbol{p}^*$. It is remarked that the parameter sets $\tilde{\boldsymbol{p}}$ and $\boldsymbol{p}^*$ can produce very similar results, but that they are in general not identical since they represent solutions to two different minimisation problems.

Table A.9 lists the optimised coefficients for both, the parameter fit and the model fit whereas Fig. A.17 shows the approximation of the temperature-discrete isothermal fit by the continuous parameter fit and model fit. While both fits yield similar parabolic progressions for b_p, a significant difference can be observed in N_p, where the parameter fit yields a nearly linear function, while the model fit leads to a pronounced parabolic shape.

The original TTT–diagram data and the recovered values from the isothermal fit, along with the predictions for the 1% and 99% lines based on the parameter fit and the model fit, are presented in Fig. A.18. As expected, the isothermal fit exactly reproduces the reference values. Both the parameter fit and the model fit are in good agreement with the original data. While the parameter fit is in slightly better agreement with values for relatively low and high temperatures, the model fit shows slightly better performance in between. Since the model fit strategy minimises a physically more meaningful error functional, it was chosen for the implementation in this work. However, based on the simulated TTT–diagram, no significant differences should be expected when applying the simpler parameter fit strategy.

A.2. Derivatives of the evolution equations

For the solution of the evolution Eqs. (68), the Jacobian

$$\frac{\partial \boldsymbol{R}_{\boldsymbol{\kappa}}}{\partial \boldsymbol{\kappa}} = \begin{bmatrix} \frac{\partial R_{\beta_{\mathrm{M}}}}{\partial \beta_{\mathrm{M}}} & \frac{\partial R_{\beta_{\mathrm{M}}}}{\partial \beta_{\mathrm{B}}} & \frac{\partial R_{\beta_{\mathrm{M}}}}{\partial x_{\mathrm{C,A}}} \\ \frac{\partial R_{\beta_{\mathrm{B}}}}{\partial \beta_{\mathrm{M}}} & \frac{\partial R_{\beta_{\mathrm{B}}}}{\partial \beta_{\mathrm{B}}} & \frac{\partial R_{\beta_{\mathrm{B}}}}{\partial x_{\mathrm{C,A}}} \\ \frac{\partial R_{x_{\mathrm{C,A}}}}{\partial \beta_{\mathrm{M}}} & \frac{\partial R_{x_{\mathrm{C,A}}}}{\partial \beta_{\mathrm{B}}} & \frac{\partial R_{x_{\mathrm{C,A}}}}{\partial x_{\mathrm{C,A}}} \end{bmatrix} \,, \tag{A.8}$$

is required. Furthermore, for the application of the implicit function theorem, the derivatives of the residual with respect to the strain increment and the temperature are necessary. Since the evolution equations do not depend on the mechanical state, as shown in Fig. 1, the relation

$$\frac{\partial \boldsymbol{R}_{\boldsymbol{\kappa}}}{\partial \Delta\boldsymbol{\varepsilon}_V} = \boldsymbol{0} \tag{A.9}$$

holds, while the temperature derivatives

$$\frac{\partial \boldsymbol{R}_{\kappa}}{\partial T} = \left[\frac{\partial R_{\beta_{\mathrm{M}}}}{\partial T} \quad \frac{\partial R_{\beta_{\mathrm{B}}}}{\partial T} \quad \frac{\partial R_{x_{\mathrm{C,A}}}}{\partial T}\right]^{\mathrm{t}} \tag{A.10}$$

are specified in the following section together with the Jacobian contributions for each evolution equation.

A.2.1. Martensite evolution

The evolution equation for martensite, Eq. (69a), reads

$$R_{\beta_{\mathrm{M}}} = \beta_{\mathrm{M}} - \beta_{\mathrm{M}}^{(n)} + \zeta_{\mathrm{M}}\left[1 - \beta_{\mathrm{M}} - \beta_{\mathrm{B}}\right] k\, \Delta T \,, \tag{A.11}$$

resulting in the Jacobian contributions

$$\frac{\partial R_{\beta_{\mathrm{M}}}}{\partial \beta_{\mathrm{M}}} = 1 - \zeta_{\mathrm{M}}\, k\, \Delta T \,, \tag{A.12}$$

$$\frac{\partial R_{\beta_{\mathrm{M}}}}{\partial \beta_{\mathrm{B}}} = -\zeta_{\mathrm{M}}\, k\, \Delta T \,, \tag{A.13}$$

$$\frac{\partial R_{\beta_{\mathrm{M}}}}{\partial x_{\mathrm{C,A}}} = \left[1 - \beta_{\mathrm{M}} - \beta_{\mathrm{B}}\right] \Delta T \left[\zeta_{\mathrm{M}} \frac{\mathrm{d}k}{\mathrm{d}x_{\mathrm{C,A}}} + \frac{\mathrm{d}\zeta_{\mathrm{M}}}{\mathrm{d}x_{\mathrm{C,A}}}\, k\right] \,, \tag{A.14}$$

and the temperature derivative

$$\frac{\partial R_{\beta_{\mathrm{M}}}}{\partial T} = \left[1 - \beta_{\mathrm{M}} - \beta_{\mathrm{B}}\right] k \left[\frac{\mathrm{d}\zeta_{\mathrm{M}}}{\mathrm{d}T}\Delta T + \zeta_{\mathrm{M}}\right] \,. \tag{A.15}$$

Inserting the derivatives of the activation function, i.e.

$$\frac{\partial \widetilde{\mathrm{H}}(T)}{\partial T} = \frac{l}{2\cosh(lT)^2} \,, \tag{A.16}$$

Table A.9
Comparison of optimal polynomial coefficients based on the parameter fit and model fit strategies.

Strategy	$p_{b,0}$	$p_{b,1}/°C^{-1}$	$p_{b,2}/°C^{-2}$	$p_{N,0}$	$p_{N,1}/°C^{-1}$	$p_{N,2}/°C^{-2}$
Parameter fit	−1.1530 e2	3.7981 e−1	−3.9804 e−4	4.8917	−6.7588 e−3	1.9972 e−6
Model fit	−1.8847 e2	8.1383 e−1	−1.0303 e−3	1.1313 e1	−4.5363 e−2	5.8965 e−5

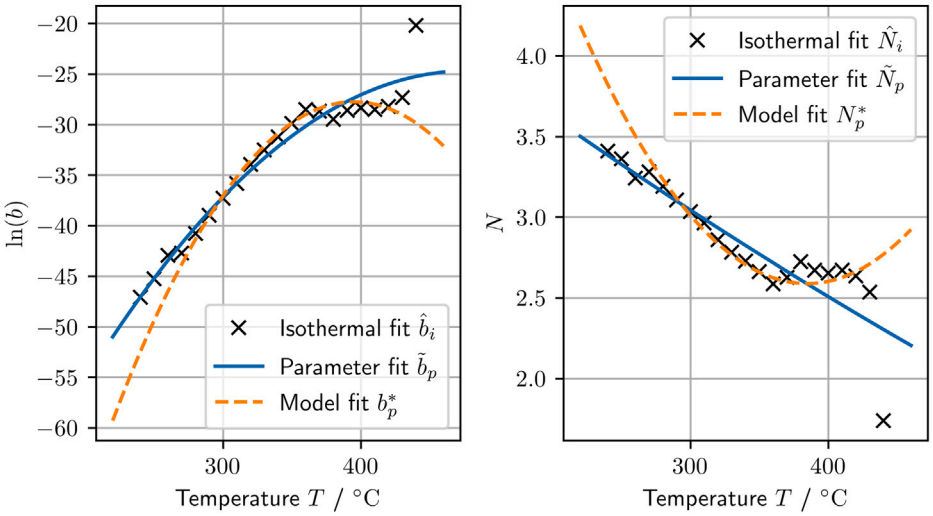

Fig. A.17. JMAK model parameters b and N obtained from different fitting strategies. The isothermal fit recovers the original diagram data up to numerical tolerances, but is only available for discrete temperatures. The parameter fit and the model fit are based on a second-order polynomial ansatz for the temperature-dependency of the parameters b and N, and represent the optimal fit of the polynomials based on the isothermal parameters and on the predicted phase fractions, respectively.

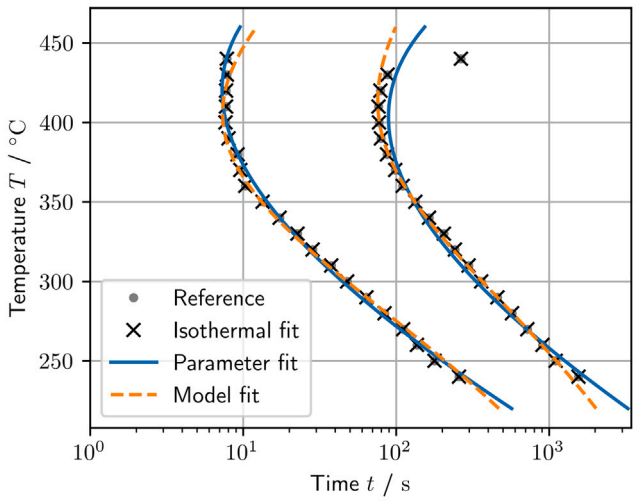

Fig. A.18. TTT–diagram with isolines for 1% and 99% bainite phase fraction. The reference data is obtained from the TTT–diagram published in Kaymak (2007), and is recovered exactly by the isothermal fit of the JMAK parameters b and N for each discrete temperature. Parameter fit and model fit strategies, based on a quadratic polynomial ansatz for the temperature-dependency of the parameters b and N, show good agreement with the data.

$$\frac{\mathrm{d}\zeta_\mathrm{M}}{\mathrm{d}x_{\mathrm{C,A}}} = \frac{\partial\zeta_\mathrm{M}}{\partial M_\mathrm{S}}\frac{\mathrm{d}M_\mathrm{S}}{\mathrm{d}x_{\mathrm{C,A}}} = \mathrm{H}\left(-\dot{T}\right)\frac{l}{2\cosh\left(l\left[M_\mathrm{S}-T\right]\right)^2}\frac{\mathrm{d}M_\mathrm{S}}{\mathrm{d}x_{\mathrm{C,A}}}\,, \tag{A.17}$$

$$\frac{\mathrm{d}\zeta_\mathrm{M}}{\mathrm{d}T} = \frac{\partial\zeta_\mathrm{M}}{\partial T} + \frac{\partial\zeta_\mathrm{M}}{\partial M_\mathrm{S}}\frac{\mathrm{d}M_\mathrm{S}}{\mathrm{d}T} = \mathrm{H}\left(-\dot{T}\right)\frac{l}{2\cosh\left(l\left[M_\mathrm{S}-T\right]\right)^2}\left[\frac{\mathrm{d}M_\mathrm{S}}{\mathrm{d}x_{\mathrm{C,A}}} - 1\right]\,, \tag{A.18}$$

leaves only the terms $\mathrm{d}M_\mathrm{S}/\mathrm{d}x_{\mathrm{C,A}}$ and $\mathrm{d}M_\mathrm{S}/\mathrm{d}k$ to be specified, which result directly from the polynomial parametrisation of the model parameters.

A.2.2. Bainite evolution

The derivatives for the bainite evolution equation will be given individually based on whether the bainite fraction has already reached the value of 1%, starting with the case that $\beta_\mathrm{B}^{(n)} \leq 1\%$. The residual evolution Eq. (69b) then reads

$$R_{\beta_\mathrm{B}} = \beta_\mathrm{B} - \beta_\mathrm{B}^{(n)} - 0.01\,\zeta_\mathrm{B}\,\Delta t/\tau\,, \tag{A.19}$$

and the derivatives with respect to the internal variables are given by

$$\frac{\partial R_{\beta_\mathrm{B}}}{\partial \beta_\mathrm{M}} = 0\,, \tag{A.20}$$

$$\frac{\partial R_{\beta_\mathrm{B}}}{\partial \beta_\mathrm{B}} = 1\,, \tag{A.21}$$

$$\frac{\partial R_{\beta_\mathrm{B}}}{\partial x_{\mathrm{C,A}}} = -0.01\frac{\Delta t}{\tau}\frac{\mathrm{d}\zeta_\mathrm{B}}{\mathrm{d}x_{\mathrm{C,A}}}\,, \tag{A.22}$$

while the temperature derivative reads

$$\frac{\partial R_{\beta_\mathrm{B}}}{\partial T} = -0.01\frac{\Delta t}{\tau}\left[\frac{\mathrm{d}\zeta_\mathrm{B}}{\mathrm{d}T} + \zeta_\mathrm{B}\left[\frac{1}{N^2}\ln\left(\frac{1}{b}\ln\left(\frac{1}{0.99}\right)\right)\frac{\mathrm{d}N}{\mathrm{d}T} + \frac{1}{b\,N}\frac{\mathrm{d}b}{\mathrm{d}T}\right]\right]\,. \tag{A.23}$$

After the nucleation is complete, i.e. when $\beta_\mathrm{B}^{(n)} > 1\%$, Eq. (69b) reads

$$R_{\beta_\mathrm{B}} = \beta_\mathrm{B} - \beta_\mathrm{B}^{(n)} - \Delta t\,\zeta_\mathrm{B}\,N\,b^{\frac{1}{N}}\left[\hat{\beta}_\mathrm{B} - \beta_\mathrm{B}\right]A^{\frac{N-1}{N}}\,, \tag{A.24}$$

where the abbreviation

$$A = \ln\left(\frac{\hat{\beta}_\mathrm{B}}{\hat{\beta}_\mathrm{B} - \beta_\mathrm{B}}\right) \tag{A.25}$$

was used to simplify the expression. In this case, the derivatives with respect to the internal variables read

$$\frac{\partial R_{\beta_B}}{\partial \beta_M} = -\Delta t\, \zeta_B \left[\frac{b}{A}\right]^{\frac{1}{N}} \left[NA - [N-1]\frac{\beta_B}{\hat{\beta}_B}\right] \frac{\mathrm{d}\hat{\beta}_B}{\mathrm{d}\beta_M} \,, \tag{A.26}$$

$$\frac{\partial R_{\beta_B}}{\partial \beta_B} = 1 - \Delta t\, \zeta_B \left[\frac{b}{A}\right]^{\frac{1}{N}} \left[N - 1 - NA + \left[NA - [N-1]\frac{\beta_B}{\hat{\beta}_B}\right] \frac{\mathrm{d}\hat{\beta}_B}{\mathrm{d}\beta_B}\right] , \tag{A.27}$$

$$\frac{\partial R_{\beta_B}}{\partial x_{C,A}} = -\Delta t \left[\frac{b}{A}\right]^{\frac{1}{N}} \left[\left[NA - [N-1]\frac{\beta_B}{\hat{\beta}_B}\right] \zeta_B \frac{\mathrm{d}\hat{\beta}_B}{\mathrm{d}x_{C,A}} + NA\left[\hat{\beta}_B - \beta_B\right] \frac{\mathrm{d}\zeta_B}{\mathrm{d}x_{C,A}}\right] . \tag{A.28}$$

The temperature derivative for this case is given by

$$\begin{aligned}\frac{\partial R_{\beta_B}}{\partial T} = -\Delta t \left[\frac{b}{A}\right]^{\frac{1}{N}} \Bigg[& NA\left[\hat{\beta}_B - \beta_B\right] \frac{\mathrm{d}\zeta_B}{\mathrm{d}T} \\ & + \zeta_B A\left[\hat{\beta}_B - \beta_B\right] \left[1 + \frac{1}{N}\ln\left(\frac{A}{b}\right)\right] \frac{\mathrm{d}N}{\mathrm{d}T} \\ & + \zeta_B \frac{A}{b}\left[\hat{\beta}_B - \beta_B\right] b^{\frac{1}{N}-1} \frac{\mathrm{d}b}{\mathrm{d}T} \\ & + \zeta_B \left[AN - [N-1]\frac{\beta_B}{\hat{\beta}_B}\right] \frac{\mathrm{d}\hat{\beta}_B}{\mathrm{d}\beta_B}\Bigg] \,.\end{aligned} \tag{A.29}$$

Simplification of the expressions requires the derivatives

$$\frac{\mathrm{d}A}{\partial \beta_M} = -\frac{\beta_B}{\hat{\beta}_B\left[\hat{\beta}_B - \beta_B\right]} \frac{\mathrm{d}\hat{\beta}_B}{\mathrm{d}\beta_M} \,, \tag{A.30}$$

$$\frac{\partial A}{\partial \beta_B} = \frac{1}{\hat{\beta}_B - \beta_B} - \frac{\beta_B}{\hat{\beta}_B\left[\hat{\beta}_B - \beta_B\right]} \frac{\mathrm{d}\hat{\beta}_B}{\mathrm{d}\beta_B} \,, \tag{A.31}$$

$$\frac{\mathrm{d}A}{\mathrm{d}x_{C,A}} = -\frac{\beta_B}{\hat{\beta}_B\left[\hat{\beta}_B - \beta_B\right]} \frac{\mathrm{d}\hat{\beta}_B}{\mathrm{d}x_{C,A}} \,, \tag{A.32}$$

$$\frac{\mathrm{d}A}{\mathrm{d}T} = -\frac{\beta_B}{\hat{\beta}_B\left[\hat{\beta}_B - \beta_B\right]} \frac{\mathrm{d}\hat{\beta}_B}{\mathrm{d}T} \,, \tag{A.33}$$

$$\begin{aligned}\frac{\mathrm{d}\tau}{\mathrm{d}T} &= \frac{\partial \tau}{\partial N}\frac{\mathrm{d}N}{\mathrm{d}T} + \frac{\partial \tau}{\partial b}\frac{\mathrm{d}b}{\mathrm{d}T} \\ &= -\frac{\tau}{N^2}\ln\left(\frac{1}{b}\ln\left(\frac{1}{0.99}\right)\right)\frac{\mathrm{d}N}{\mathrm{d}T} - \frac{\tau}{b\,N}\frac{\mathrm{d}b}{\mathrm{d}T} \,.\end{aligned} \tag{A.34}$$

To complete the implementation, the derivatives of the maximum reachable bainite fraction

$$\frac{\mathrm{d}\hat{\beta}_B}{\mathrm{d}\beta_M} = -\mathrm{f} \,, \tag{A.35}$$

$$\frac{\mathrm{d}\hat{\beta}_B}{\mathrm{d}\beta_B} = 1 - \mathrm{f} \,, \tag{A.36}$$

$$\frac{\mathrm{d}\hat{\beta}_B}{\mathrm{d}x_{C,A}} = \beta_A \frac{\mathrm{d}\,\mathrm{f}}{\mathrm{d}x_{C,A}} = -\beta_A \frac{x^*_{C,A}}{x_{C,B} - x^*_{C,A}} \,, \tag{A.37}$$

$$\frac{\mathrm{d}\hat{\beta}_B}{\mathrm{d}T} = \beta_A \frac{\mathrm{d}\,\mathrm{f}}{\mathrm{d}T} = \beta_A \frac{\mathrm{d}\,\mathrm{f}}{\mathrm{d}x^*_{C,A}}\frac{\mathrm{d}x^*_{C,A}}{\mathrm{d}T} = \beta_A \frac{x_{C,A} - x_{C,B}}{\left[x_{C,B} - x^*_{C,A}\right]^2}\frac{p_{B_S,0}}{p_{B_S,1}} \,, \tag{A.38}$$

and of the activation function

$$\frac{\mathrm{d}\zeta_B}{\mathrm{d}\beta_M} = 0 \,, \tag{A.39}$$

$$\frac{\mathrm{d}\zeta_B}{\mathrm{d}\beta_B} = 0 \,, \tag{A.40}$$

$$\frac{\mathrm{d}\zeta_B}{\mathrm{d}x_{C,A}} = \frac{\partial \zeta_B}{\partial B_S}\frac{\mathrm{d}B_S}{\mathrm{d}x_{C,A}} = \frac{l}{2\cosh\left(l\left[B_S - T\right]\right)^2}\frac{\mathrm{d}B_S}{\mathrm{d}x_{C,A}} \,, \tag{A.41}$$

$$\frac{\mathrm{d}\zeta_B}{\mathrm{d}T} = \frac{\partial \zeta_B}{\partial T} + \frac{\partial \zeta_B}{\partial B_S}\frac{\mathrm{d}B_S}{\mathrm{d}T} = \frac{l}{2\cosh\left(l\left[B_S - T\right]\right)^2}\left[\frac{\mathrm{d}B_S}{\mathrm{d}x_{C,A}} - 1\right] \tag{A.42}$$

are required.

A.2.3. Evolution of austenite phase carbon content

Based on the residual format of the carbon mass balance presented in Eq. (69c), i.e.

$$R_{x_{C,A}} = \left[1 - \beta_M - \beta_B\right]\left[x_{C,A} - x^{(n)}_{C,A}\right] - \left[\beta_B - \beta^{(n)}_B\right]\left[x_{C,A} - x_{C,B}\right] \,, \tag{A.43}$$

the Jacobian contributions read

$$\frac{\partial R_{x_{C,A}}}{\partial \beta_M} = -\left[x_{C,A} - x^{(n)}_{C,A}\right] \tag{A.44}$$

$$\frac{\partial R_{x_{C,A}}}{\partial \beta_B} = -\left[x_{C,A} - x^{(n)}_{C,A}\right] - \left[x_{C,A} - x_{C,B}\right] \tag{A.45}$$

$$\frac{\partial R_{x_{C,A}}}{\partial x_{C,A}} = \left[1 - \beta_M - \beta_B\right] - \left[\beta_B - \beta^{(n)}_B\right] \,, \tag{A.46}$$

while the temperature derivative is given by

$$\frac{\partial R_{x_{C,A}}}{\partial T} = 0 \,. \tag{A.47}$$

A.3. Derivatives of stresses

For the finite element implementation, the derivatives of the stress increment $\Delta\boldsymbol{\sigma}_V$ with respect to the strain increment $\Delta\boldsymbol{\varepsilon}_V$, the temperature T and the internal variables $\boldsymbol{\kappa}$ are required.

Recalling Eqs. (70) and (71), i.e.

$$\Delta\boldsymbol{\sigma}_V = \mathbf{E}_V \cdot \left[\left[\boldsymbol{\varepsilon}^{\mathrm{el}}_V\right]^{(n)} + \Delta\boldsymbol{\varepsilon}^{\mathrm{el}}_V\right] - \boldsymbol{\sigma}^{(n)}_V = \mathbf{E}_V \cdot \boldsymbol{\varepsilon}^{\mathrm{el}}_V - \boldsymbol{\sigma}^{(n)}_V \tag{A.48}$$

and

$$\Delta\boldsymbol{\varepsilon}^{\mathrm{el}}_V = \Delta\boldsymbol{\varepsilon}_V - \alpha\Delta T\,\boldsymbol{I}_V - \Delta\gamma\,\boldsymbol{I}_V \,, \tag{A.49}$$

the partial derivative with respect to the strain increment reads

$$\frac{\partial \Delta\boldsymbol{\sigma}_V}{\partial \Delta\boldsymbol{\varepsilon}_V} = \mathbf{E}_V \,. \tag{A.50}$$

The temperature derivative is given by

$$\frac{\partial \Delta\boldsymbol{\sigma}_V}{\partial T} = \frac{\partial \mathbf{E}_V}{\partial T} \cdot \boldsymbol{\varepsilon}^{\mathrm{el}}_V + \mathbf{E}_V \cdot \frac{\partial \Delta\boldsymbol{\varepsilon}^{\mathrm{el}}_V}{\partial T} \,, \tag{A.51}$$

where the temperature derivative of the elastic tensor is given by

$$\frac{\partial \mathbf{E}_V}{\partial T} = \sum_i \left[\frac{\partial \mathbf{E}_V}{\partial E_i}\frac{\mathrm{d}E_i}{\mathrm{d}T} + \frac{\partial \mathbf{E}_V}{\partial \nu_i}\frac{\mathrm{d}\nu_i}{\mathrm{d}T}\right] \tag{A.52}$$

with

$$\frac{\partial \mathsf{E}_{ijkl}}{\partial E} = \frac{\nu}{[1-\nu][1-2\nu]}\delta_{ij}\,\delta_{kl} + \frac{1}{2(1+\nu)}\left[\delta_{ik}\,\delta_{jl} + \delta_{il}\,\delta_{jk}\right] \,, \tag{A.53}$$

$$\frac{\partial \mathsf{E}_{ijkl}}{\partial \nu} = E\frac{2\nu^2 + 1}{2\nu^2 + \nu - 1}\delta_{ij}\,\delta_{kl} - \frac{E}{2[1+\nu]^2}\left[\delta_{ik}\,\delta_{jl} + \delta_{il}\,\delta_{jk}\right] \,. \tag{A.54}$$

Derivation of the elastic strain increment with respect to the temperature yields

$$\frac{\partial \Delta\boldsymbol{\varepsilon}_V}{\partial T} = -\left[\alpha + \sum_i \beta_i \frac{\partial \alpha_i}{\partial T}\Delta T + \sum_i \beta_i \frac{\partial \gamma_i}{\partial T}\right] \boldsymbol{I}_V \,. \tag{A.55}$$

The derivatives $\mathrm{d}E_i/\mathrm{d}T$, $\mathrm{d}\nu_i/\mathrm{d}T$, $\mathrm{d}\alpha_i/\mathrm{d}T$, and $\mathrm{d}\gamma_i/\mathrm{d}T$ are obtained from the respective polynomial parametrisations.

For the derivative with respect to the internal variables $\boldsymbol{\kappa}$, which has the structure

$$\frac{\partial \Delta\boldsymbol{\sigma}_V}{\partial \boldsymbol{\kappa}} = \left[\frac{\partial \Delta\boldsymbol{\sigma}_V}{\partial \beta_M} \quad \frac{\partial \Delta\boldsymbol{\sigma}_V}{\partial \beta_B} \quad \frac{\partial \Delta\boldsymbol{\sigma}_V}{\partial x_{C,A}}\right] \,, \tag{A.56}$$

the individual terms read

$$\frac{\partial \Delta\boldsymbol{\sigma}_V}{\partial \beta_M} = \frac{\partial \mathbf{E}_V}{\partial \beta_M} \cdot \boldsymbol{\varepsilon}^{\mathrm{el}}_V + \mathbf{E}_V \cdot \frac{\partial \Delta\boldsymbol{\varepsilon}^{\mathrm{el}}_V}{\partial \beta_M} \,, \tag{A.57}$$

$$\frac{\partial \Delta\boldsymbol{\sigma}_V}{\partial \beta_B} = \frac{\partial \mathbf{E}_V}{\partial \beta_B} \cdot \boldsymbol{\varepsilon}^{\mathrm{el}}_V + \mathbf{E}_V \cdot \frac{\partial \Delta\boldsymbol{\varepsilon}^{\mathrm{el}}_V}{\partial \beta_B} \,, \tag{A.58}$$

$$\frac{\partial \Delta\boldsymbol{\sigma}_V}{\partial x_{C,A}} = \mathbf{0} \,, \tag{A.59}$$

with

$$\frac{\partial \mathbf{E}_V}{\partial \beta_\mathrm{M}} = \mathbf{E}_{\mathrm{M},V} - \mathbf{E}_{\mathrm{A},V} \ , \tag{A.60}$$

$$\frac{\partial \mathbf{E}_V}{\partial \beta_\mathrm{B}} = \mathbf{E}_{\mathrm{B},V} - \mathbf{E}_{\mathrm{A},V} \ , \tag{A.61}$$

$$\frac{\partial \Delta\boldsymbol{\varepsilon}_V^{\mathrm{el}}}{\partial \beta_\mathrm{M}} = -\left[\alpha_\mathrm{M} - \alpha_\mathrm{A}\right] \Delta T \, \boldsymbol{I}_V - \left[\gamma_\mathrm{M} - \gamma_\mathrm{A}\right] \boldsymbol{I}_V \ , \tag{A.62}$$

$$\frac{\partial \Delta\boldsymbol{\varepsilon}_V^{\mathrm{el}}}{\partial \beta_\mathrm{B}} = -\left[\alpha_\mathrm{B} - \alpha_\mathrm{A}\right] \Delta T \, \boldsymbol{I}_V - \left[\gamma_\mathrm{B} - \gamma_\mathrm{A}\right] \boldsymbol{I}_V \ . \tag{A.63}$$

A.4. Derivatives of the heat generation rate

The discrete heat generation rate was derived in Eq. (75) as

$$r_{pl} = \frac{\beta_\mathrm{M} - \beta_\mathrm{M}^{(n)}}{\Delta t} \rho \, \Delta h_{\mathrm{A}\to\mathrm{M}} + \frac{\beta_\mathrm{B} - \beta_\mathrm{B}^{(n)}}{\Delta t} \rho \, \Delta h_{\mathrm{A}\to\mathrm{B}} \ , \tag{A.64}$$

so derivation with respect to the strain increment trivially yields

$$\frac{\partial r_{pl}}{\partial \Delta\boldsymbol{\varepsilon}_V} = \mathbf{0} \ . \tag{A.65}$$

The temperature derivative is given by

$$\frac{\partial r_{pl}}{\partial T} = \frac{\beta_\mathrm{M} - \beta_\mathrm{M}^{(n)}}{\Delta t} \frac{\mathrm{d}(\rho \, \Delta h_{\mathrm{A}\to\mathrm{M}})}{\mathrm{d}T} + \frac{\beta_\mathrm{B} - \beta_\mathrm{B}^{(n)}}{\Delta t} \frac{\mathrm{d}(\rho \, \Delta h_{\mathrm{A}\to\mathrm{B}})}{\mathrm{d}T} \ , \tag{A.66}$$

while the derivation with respect to the internal variables yields

$$\frac{\partial r_{pl}}{\partial \beta_\mathrm{M}} = \frac{\rho \, \Delta h_{\mathrm{A}\to\mathrm{M}}}{\Delta t} \ , \tag{A.67}$$

$$\frac{\partial r_{pl}}{\partial \beta_\mathrm{B}} = \frac{\rho \, \Delta h_{\mathrm{A}\to\mathrm{B}}}{\Delta t} \ , \tag{A.68}$$

$$\frac{\partial r_{pl}}{\partial x_{\mathrm{C,A}}} = 0 \ . \tag{A.69}$$

All remaining temperature derivatives, i.e. $\mathrm{d}(\rho \, \Delta h_{\mathrm{A}\to\mathrm{M}})/\mathrm{d}T$ and $\mathrm{d}(\rho \, \Delta h_{\mathrm{A}\to\mathrm{B}})/\mathrm{d}T$, follow from the polynomial parametrisations.

Data availability

Source code and data available at https://github.com/InstituteOfMechanics/Phase_Trafos_Carbon_Repartitioning.

References

Abeyaratne, R., Knowles, J.K., 1993. A continuum model of a thermoelastic solid capable of undergoing phase transitions. J. Mech. Phys. Solids 41 (3), 541–571. http://dx.doi.org/10.1016/0022-5096(93)90048-K.

Amirmaleki, M., Samei, J., Green, D.E., Van Riemsdijk, I., Stewart, L., 2016. 3D micromechanical modeling of dual phase steels using the representative volume element method. Mech. Mater. 101, 27–39. http://dx.doi.org/10.1016/j.mechmat.2016.07.011.

Andersson, B., Ahlström, J., Ekh, M., Josefson, B.L., 2022. Homogenization based macroscopic model of phase transformations and cyclic plasticity in pearlitic steel. J. Therm. Stresses 45 (6), 470–492. http://dx.doi.org/10.1080/01495739.2022.2056557.

Avrami, M., 1939. Kinetics of phase change. I General theory. J. Chem. Phys. 7 (12), 1103–1112. http://dx.doi.org/10.1063/1.1750380.

Avrami, M., 1940. Kinetics of phase change. II Transformation-time relations for random distribution of nuclei. J. Chem. Phys. 8 (2), 212–224. http://dx.doi.org/10.1063/1.1750631.

Avrami, M., 1941. Granulation, phase change, and microstructure kinetics of phase change. III. J. Chem. Phys. 9 (2), 177–184. http://dx.doi.org/10.1063/1.1750872.

Barmak, K., 2018. A commentary on: "Reaction kinetics in processes of nucleation and growth"*. Met. Mater. Trans. B 49 (6), 3616–3680. http://dx.doi.org/10.1007/s11663-010-9421-1.

Benrabah, I.-E., Brechet, Y., Hutchinson, C., Zurob, H., 2024. On the origin of carbon supersaturation in bainitic ferrite. Scr. Mater. 250, 116182. http://dx.doi.org/10.1016/j.scriptamat.2024.116182.

Bhattacharyya, A., Weng, G., 1994. An energy criterion for the stress-induced martensitic transformation in a ductile system. J. Mech. Phys. Solids 42 (11), 1699–1724. http://dx.doi.org/10.1016/0022-5096(94)90068-X.

Boccardo, A., Dardati, P., Celentano, D., Godoy, L., 2017. Austempering heat treatment of ductile iron: computational simulation and experimental validation. Finite Elem. Anal. Des. 134, 82–91. http://dx.doi.org/10.1016/j.finel.2017.06.002.

Çetinel, H., Toparlı, M., Özsoyeller, L., 2000. A finite element based prediction of the microstructural evolution of steels subjected to the tempcore process. Mech. Mater. 32 (6), 339–347. http://dx.doi.org/10.1016/S0167-6636(00)00009-0.

Caballero, F., 2012. Carbide-free bainite in steels. In: Pereloma, E., Edmonds, D. (Eds.), Phase Transformations in Steels. Elsevier, pp. 436–467. http://dx.doi.org/10.1533/9780857096104.3.436.

Cui, W., San-Martín, D., Rivera-Díaz-del-Castillo, P.E., 2017. Towards efficient microstructural design and hardness prediction of bearing steels — an integrated experimental and numerical study. Mater. Des. 133, 464–475. http://dx.doi.org/10.1016/j.matdes.2017.08.013.

Dassault Systèmes, 2023. Abaqus documentation, version 2023. https://www.3ds.com/.

Davenport, E.S., Bain, E.C., 1970. Transformation of austenite at constant subcritical temperatures. Met. Trans. 1 (12), 3503–3530. http://dx.doi.org/10.1007/BF03037892.

De Oliveira, W.P., Savi, M.A., Pacheco, P.M.C.L., De Souza, L.F.G., 2010. Thermomechanical analysis of steel cylinders quenching using a constitutive model with diffusional and non-diffusional phase transformations. Mech. Mater. 42 (1), 31–43. http://dx.doi.org/10.1016/j.mechmat.2009.09.006.

Denis, S., Gautier, E., Simon, A., Beck, G., 1985. Stress–phase-transformation interactions – basic principles, modelling, and calculation of internal stresses. Mater. Sci. Technol. 1 (10), 805–814. http://dx.doi.org/10.1179/mst.1985.1.10.805.

Denis, S., Sjöström, S., Simon, A., 1987. Coupled temperature, stress, phase transformation calculation model numerical illustration of the internal stresses evolution during cooling of a eutectoid carbon steel cylinder. Met. Trans. A 18 (7), 1203–1212. http://dx.doi.org/10.1007/BF02647190.

Deutsches Institut für Normung e.V., 2023. EN ISO 683-17:2023: heat-treated steels, alloy steels and free-cutting steels - part 17: ball and roller bearing steels.

Fernandes, F.M.B., Denis, S., Simon, A., 1985. Mathematical model coupling phase transformation and temperature evolution during quenching of steels. Mater. Sci. Technol. 1 (10), 838–844. http://dx.doi.org/10.1179/mst.1985.1.10.838.

Fernández-Pisón, P., Vishnu, A., Vadillo, G., Rodríguez-Martínez, J., 2024. Modeling strain-induced martensitic transformation in austenitic stainless steels subjected to cryogenic temperatures using incremental mean-field homogenization schemes. Mech. Mater. 189, 104891. http://dx.doi.org/10.1016/j.mechmat.2023.104891.

Fielding, L.C.D., 2013. The bainite controversy. Mater. Sci. Technol. 29 (4), 383–399. http://dx.doi.org/10.1179/1743284712Y.0000000157.

Fischer, F., 1990. A micromechanical model for transformation plasticity in steels. Acta Met. Mater. 38 (8), 1535–1546. http://dx.doi.org/10.1016/0956-7151(90)90121-V.

Furlan, T., Stollberg, J., Menzel, A., 2025. Paraqus: exporting finite element simulation results from abaqus to VTK. J. Open Sour. Softw. 10 (106), 5729. http://dx.doi.org/10.21105/joss.05729, URL: https://github.com/InstituteOfMechanics/Paraqus.

Ganghoffer, J., Simonsson, K., 1998. A micromechanical model of the martensitic transformation. Mech. Mater. 27 (3), 125–144. http://dx.doi.org/10.1016/S0167-6636(97)00044-6.

Gür, C.H., Şimşir, C., 2012. Simulation of quenching: a review. Mater. Perform. Charact. 1 (1), 104479. http://dx.doi.org/10.1520/MPC104479.

Gür, C., Tekkaya, A., 2001. Numerical investigation of non-homogeneous plastic deformation in quenching process. Mater. Sci. Eng.: A 319–321, 164–169. http://dx.doi.org/10.1016/S0921-5093(01)01064-4.

Gurtin, M.E., 1983. Two-phase deformations of elastic solids. Arch. Ration. Mech. Anal. 84 (1), 1–29. http://dx.doi.org/10.1007/BF00251547.

Hazar, S., Alfredsson, B., Lai, J., 2018. Mechanical modeling of coupled plasticity and phase transformation effects in a martensitic high strength bearing steel. Mech. Mater. 117, 41–57. http://dx.doi.org/10.1016/j.mechmat.2017.10.001.

Hellebrand, S., Brands, D., Schröder, J., 2023. On the three-dimensional numerical analysis of residual stresses on two scales in hot bulk forming parts. PAMM 23 (3), e202300087. http://dx.doi.org/10.1002/pamm.202300087.

Hunkel, M., 2020. Tempering effects of athermal martensite during quenching and reheating of a SAE 52100 bearing steel. Mater. Sci. Eng.: A 790, 139601. http://dx.doi.org/10.1016/j.msea.2020.139601.

Huyan, F., Hedström, P., Borgenstam, A., 2015. Modelling of the fraction of martensite in low-alloy steels. Mater. Today: Proc. 2, S561–S564. http://dx.doi.org/10.1016/j.matpr.2015.07.347.

Ingber, J., Kunert, M., 2022. Prediction of the martensite start temperature in high-carbon steels. Steel Res. Int. 93 (5), 2100576. http://dx.doi.org/10.1002/srin.202100576.

James, R., 1986. Displacive phase transformations in solids. J. Mech. Phys. Solids 34 (4), 359–394. http://dx.doi.org/10.1016/0022-5096(86)90008-6.

Jia, T., Militzer, M., Liu, Z.Y., 2010. General method of phase transformation modeling in advanced high strength steels. ISIJ Int. 50 (4), 583–590. http://dx.doi.org/10.2355/isijinternational.50.583.

Johnson, W.A., Mehl, R.F., 1939. Reaction kinetics in processes of nucleation and growth. Trans. Am. Inst. Min. Met. Eng. 135, 416–442.

Junker, P., Hackl, K., 2014. A thermo-mechanically coupled field model for shape memory alloys. Contin. Mech. Thermodyn. 26 (6), 859–877. http://dx.doi.org/10.1007/s00161-014-0345-x.

Kaymak, Y., 2007. Simulation of Metal Quenching Processes for the Minimization of Distortion and Stresses (Ph.D. thesis). Otto-von-Guericke-Universität Magdeburg, http://dx.doi.org/10.25673/4872.

Koistinen, D., Marburger, R., 1959. A general equation prescribing the extent of the austenite-martensite transformation in pure iron-carbon alloys and plain carbon steels. Acta Metall. 7 (1), 59–60. http://dx.doi.org/10.1016/0001-6160(59)90170-1.

Kolmogorov, A.N., 1937. On the statistical theory of crystallization of metals [in Russian]. Izv. Akad. Nauk. SSSR Ser. Math. 3, 355–359.

Kolmogorov, A.N., 1992. On the statistical theory of metal crystallization [english translation]. In: Shiryayev, A.N. (Ed.), Selected Works of a.N. Kolmogorov. Volume II, Probability Theory and Mathematical Statistics. Springer Netherlands, Dordrecht, pp. 188–192.

Kozeschnik, E., 2022. Mean-field microstructure kinetics modeling. In: Caballero, F.G. (Ed.), Encyclopedia of Materials: Metals and Alloys. Elsevier, pp. 521–526. http://dx.doi.org/10.1016/B978-0-12-819726-4.00055-7.

Lagoudas, D., Hartl, D., Chemisky, Y., Machado, L., Popov, P., 2012. Constitutive model for the numerical analysis of phase transformation in polycrystalline shape memory alloys. Int. J. Plast. 32–33, 155–183. http://dx.doi.org/10.1016/j.ijplas.2011.10.009.

Leblond, J., Devaux, J., 1984. A new kinetic model for anisothermal metallurgical transformations in steels including effect of austenite grain size. Acta Metall. 32 (1), 137–146. http://dx.doi.org/10.1016/0001-6160(84)90211-6.

Leblond, J., Mottet, G., Devaux, J., 1986. A theoretical and numerical approach to the plastic behaviour of steels during phase transformations—I. Derivation of general relations. J. Mech. Phys. Solids 34 (4), 395–409. http://dx.doi.org/10.1016/0022-5096(86)90009-8.

Leblond, J.-B., Mottet, G., Devaux, J., Devaux, J.-C., 1985. Mathematical models of anisothermal phase transformations in steels, and predicted plastic behaviour. Mater. Sci. Technol. 1 (10), 815–822. http://dx.doi.org/10.1179/mst.1985.1.10.815.

Lee, S.-J., Van Tyne, C.J., 2012. A kinetics model for martensite transformation in plain carbon and low-alloyed steels. Met. Mater. Trans. A 43 (2), 422–427. http://dx.doi.org/10.1007/s11661-011-0872-z.

Li, H., Gai, K., He, L., Zhang, C., Cui, H., Li, M., 2016. Non-isothermal phase-transformation kinetics model for evaluating the austenization of 55CrMo steel based on Johnson–Mehl–Avrami equation. Mater. Des. 92, 731–741. http://dx.doi.org/10.1016/j.matdes.2015.12.110.

Li, Y., Jiang, Z., Wang, P., Li, D., Li, Y., 2023. Effect of a modified quenching on impact toughness of 52100 bearing steels. J. Mater. Sci. Technol. 160, 96–108. http://dx.doi.org/10.1016/j.jmst.2023.02.057.

Li, Y., Xu, M., Jin, Y., Lu, H., 2015. Finite-element simulation of low-alloy high strength steel welding incorporating improved martensite transformation kinetics and recrystalization annealing. ISIJ Int. 55 (7), 1448–1453. http://dx.doi.org/10.2355/isijinternational.55.1448.

Mahnken, R., Schneidt, A., Antretter, T., 2009. Macro modelling and homogenization for transformation induced plasticity of a low-alloy steel. Int. J. Plast. 25 (2), 183–204. http://dx.doi.org/10.1016/j.ijplas.2008.03.005.

Mirhosseini, S., Perdahcıoğlu, E., Atzema, E., Van Den Boogaard, A., 2022. Effect of temperature and heat generation on martensitic phase transformation in DH steels. Results Mater. 14, 100281. http://dx.doi.org/10.1016/j.rinma.2022.100281.

Müller, I., 1989. On the size of the hysteresis in pseudoelasticity. Contin. Mech. Thermodyn. 1 (2), 125–142. http://dx.doi.org/10.1007/BF01141998.

Mustak, O., Evcil, E., Simsir, C., 2016. Simulation of through-hardening of SAE 52100 steel bearings – part i: determination of material properties. Mater. Werkst. 47 (8), 735–745. http://dx.doi.org/10.1002/mawe.201600607.

Noll, I., Bartel, T., Menzel, A., 2024. A thermodynamically consistent phase transformation model for multiphase alloys: application to Ti6Al4V in laser powder bed fusion processes. Comput. Mech. http://dx.doi.org/10.1007/s00466-024-02479-z.

Oka, M., Okamoto, H., Ishida, K., 1990. Transformation of lower bainite in hypereutectoid steels. Met. Trans. A 21 (3), 845–851. http://dx.doi.org/10.1007/BF02656568.

Ostwald, R., Bartel, T., Menzel, A., 2012. Phase-transformations interacting with plasticity – a micro-sphere model applied to TRIP steel. Comput. Mater. Sci. 64, 12–16. http://dx.doi.org/10.1016/j.commatsci.2012.05.015.

Ostwald, R., Bartel, T., Menzel, A., 2015. An energy-barrier-based computational micro-sphere model for phase-transformations interacting with plasticity. Comput. Methods Appl. Mech. Engrg. 293, 232–265. http://dx.doi.org/10.1016/j.cma.2015.04.008.

Ravi, A.M., Navarro-López, A., Sietsma, J., Santofimia, M.J., 2020. Influence of martensite/austenite interfaces on bainite formation in low-alloy steels below M_s. Acta Mater. 188, 394–405. http://dx.doi.org/10.1016/j.actamat.2020.02.003.

Ravi, A.M., Sietsma, J., Santofimia, M.J., 2016. Exploring bainite formation kinetics distinguishing grain-boundary and autocatalytic nucleation in high and low-Si steels. Acta Mater. 105, 155–164. http://dx.doi.org/10.1016/j.actamat.2015.11.044.

Reti, T., Fried, Z., Felde, I., 2001. Computer simulation of steel quenching process using a multi-phase transformation model. Comput. Mater. Sci. 22 (3–4), 261–278. http://dx.doi.org/10.1016/S0927-0256(01)00240-3.

Retzl, P., Zamberger, S., Kozeschnik, E., 2021. Computational analysis of austenite film thickness and C-redistribution in carbide-free bainite. Mater. Res. Exp. 8 (7), 076502. http://dx.doi.org/10.1088/2053-1591/ac0d6f.

Rezaei, J., Parsa, M.H., Mirzadeh, H., 2023. Phase transformation kinetics of high-carbon steel during continuous heating. J. Mater. Res. Technol. 27, 2524–2537. http://dx.doi.org/10.1016/j.jmrt.2023.10.089.

Rohatgi, A., 2024. WebPlotDigitizer. https://automeris.io/.

Said Schicchi, D., Caggiano, A., Hunkel, M., Koenders, E.A.B., 2019. Thermodynamically consistent multiscale formulation of a thermo-mechanical problem with phase transformations. Contin. Mech. Thermodyn. 31 (1), 273–299. http://dx.doi.org/10.1007/s00161-018-0682-2.

Santofimia, M.J., Caballero, F.G., Capdevila, C., García-Mateo, C., De Andrés, C.G., 2006. Evaluation of displacive models for bainite transformation kinetics in steels. Mater. Trans. 47 (6), 1492–1500. http://dx.doi.org/10.2320/matertrans.47.1492.

Scheil, E., 1935. Anlaufzeit der austenitumwandlung. Arch. Eisenhüttenwesen 8 (12), 565–567. http://dx.doi.org/10.1002/srin.193500186.

Schneidt, A., Mahnken, R., 2008. Macromodelling of transformation induced plasticity combined with viscoplasticity for low-alloy steels. Steel Res. Int. 79 (2), 116–123. http://dx.doi.org/10.1002/srin.200806326.

Silva, E.P., Pacheco, P.M.C.L., Savi, M.A., 2004. On the thermo-mechanical coupling in austenite–martensite phase transformation related to the quenching process. Int. J. Solids Struct. 41 (3–4), 1139–1155. http://dx.doi.org/10.1016/j.ijsolstr.2003.09.049.

Şimşir, C., Gür, C.H., 2008. 3D FEM simulation of steel quenching and investigation of the effect of asymmetric geometry on residual stress distribution. J. Mater. Process. Technol. 207 (1–3), 211–221. http://dx.doi.org/10.1016/j.jmatprotec.2007.12.074.

Şimşir, C., Gür, C.H., 2016. Quenching: simulation. In: Colás, R., Totten, G.E. (Eds.), Encyclopedia of Iron, Steel, and their Alloys, first ed. CRC Press, Boca Raton, pp. 2892–2939. http://dx.doi.org/10.1081/E-EISA.

Suwanpinij, P., Li, X., Prahl, U., Bleck, W., 2017. Modeling bainite transformation and retained austenite in hot rolled TRIP steel by instantaneous carbon enrichment. Steel Res. Int. 88 (12), 1700122. http://dx.doi.org/10.1002/srin.201700122.

Taleb, L., 2014. Transformation-induced plasticity (TRIP). In: Hetnarski, R.B. (Ed.), Encyclopedia of Thermal Stresses. Springer Netherlands, Dordrecht, pp. 6153–6163. http://dx.doi.org/10.1007/978-94-007-2739-7_858.

Taleb, L., Petit, S., 2006. New investigations on transformation induced plasticity and its interaction with classical plasticity. Int. J. Plast. 22 (1), 110–130. http://dx.doi.org/10.1016/j.ijplas.2005.03.012.

Tjahjanto, D.D., Turteltaub, S., Suiker, A.S.J., 2008. Crystallographically based model for transformation-induced plasticity in multiphase carbon steels. Contin. Mech. Thermodyn. 19 (7), 399–422. http://dx.doi.org/10.1007/s00161-007-0061-x.

Toloui, M., Militzer, M., 2018. Phase field modeling of the simultaneous formation of bainite and ferrite in TRIP steel. Acta Mater. 144, 786–800. http://dx.doi.org/10.1016/j.actamat.2017.11.047.

Tsuzaki, K., Maki, T., 1995. Some aspects of bainite transformation in Fe-based alloys. Le J. Phys. IV 05 (C8), C8–61–C8–70. http://dx.doi.org/10.1051/jp4:1995807.

Tzitzelkov, I., Hougardy, H.P., Rose, A., 1974. Mathematische Beschreibung des Zeit-Temperatur-Umwandlung-Schaubildes für isothermische Umwandlung und kontinuierliche Abkühlung. Arch. Eisenhüttenwesen 45 (8), 525–532. http://dx.doi.org/10.1002/srin.197403916.

Van Bohemen, S.M.C., 2012. Bainite and martensite start temperature calculated with exponential carbon dependence. Mater. Sci. Technol. 28 (4), 487–495. http://dx.doi.org/10.1179/1743284711Y.0000000097.

Van Bohemen, S., 2019. Bainite growth retardation due to mechanical stabilisation of austenite. Mater. 7, 100384. http://dx.doi.org/10.1016/j.mtla.2019.100384.

Van Bohemen, S., Sietsma, J., 2009. Martensite formation in partially and fully austenitic plain carbon steels. Met. Mater. Trans. A 40 (5), 1059–1068. http://dx.doi.org/10.1007/s11661-009-9796-2.

Wei, W., Retzl, P., Kozeschnik, E., Erwin Povoden-Karadeniz, 2021. A semi-physical α-β model on bainite transformation kinetics and carbon partitioning. Acta Mater. 207, 116701. http://dx.doi.org/10.1016/j.actamat.2021.116701.

Woodard, P.R., Chandrasekar, S., Yang, H.T.Y., 1999. Analysis of temperature and microstructure in the quenching of steel cylinders. Met. Mater. Trans. B 30 (4), 815–822. http://dx.doi.org/10.1007/s11663-999-0043-4.